

Facultad
de
Ciencias

PRIMORDIAL BLACK HOLES IN GALAXIES

(AGUJEROS NEGROS PRIMORDIALES EN
GALAXIAS)

Trabajo de Fin de Grado
para acceder al
GRADO EN FÍSICA

Autor: Daniel Isla Mazón

Director: Luis Julian Goicoechea

Codirector: Vyacheslav Shalyapin

Septiembre - 2024

Agradecimientos

Con este trabajo, concluye una etapa muy importante en mi vida, una que sin duda ha estado llena de retos y aprendizajes, pero que también me ha permitido crecer como persona. Por ello, me gustaría agradecer a todas esas personas que me han acompañado durante este proceso.

Me gustaría agradecer en primer lugar a mis padres, mi gran apoyo durante toda la vida, que sin duda ha resultado crucial a lo largo de estos cinco años, gracias por todo, sin vosotros no lo habría logrado.

Por otro lado, también me gustaría expresar mi agradecimiento a Luis, por tu entrega, apoyo y paciencia durante la elaboración de este proyecto. Tu experiencia y orientación han sido cruciales, y valoro enormemente tu cercanía y la manera en que has hecho que todo fuera mucho más fácil. Muchas gracias por proponerme un tema tan interesante, y por contagiarme tu entusiasmo hacia la investigación, algo que espero sea muy importante en mi futuro, y en parte será gracias a ti.

Agradezco también a todos y cada uno de los profesores del grado que me han dado clase durante estos cinco años, así como a mis amigos, gracias a todos aquellos que me habeis acompañado a lo largo de estos años, gracias por todos esos momentos.

Abstract

Although dark matter in galaxies may consist of elementary particles different from those that conform ordinary matter and that would be smoothly distributed (still undetected), primordial black holes (PBHs) formed after the initial Big Bang are also candidates to account for a certain fraction of mass in galaxies. In this project, we consider different populations of PBHs in the main lens galaxy of the doubly imaged gravitationally lensed quasar FBQ 0951+2635. The observed microlensing variability of the quasar images is compared with the microlensing variability generated by stars and PBHs in the lens galaxy at redshift $z \sim 0.3$, obtaining strong constraints on possible PBH populations in the non-local early-type galaxy acting as a gravitational lens.

Keywords: Gravitational lensing: strong, gravitational lensing: micro, quasars: individual: 0951+2633, galaxies: halos, dark matter, primordial black holes.

Resumen

Aunque la materia oscura en las galaxias podría estar compuesta por partículas elementales diferentes de las que forman la materia ordinaria y que estarían distribuidas de manera homogénea (aún no detectadas), los agujeros negros primordiales (PBHs), formados después del Big Bang inicial, también son candidatos para representar una cierta fracción de la masa en las galaxias. En este proyecto, consideramos diferentes poblaciones de PBHs en la galaxia lente principal del cuásar FBQ 0951+2635, que presenta dos imágenes debido al efecto lente gravitacional. La variabilidad observada por efecto de microlente de las imágenes del cuásar es comparada con la variabilidad generada por estrellas y PBHs en la galaxia lente a un redshift $z \sim 0.3$, obteniendo importantes restricciones sobre las posibles poblaciones de PBHs en la galaxia de tipo temprano no local que actúa como lente gravitacional.

Palabras clave: Lente gravitacional: fuerte, lente gravitacional: microlente, cuásares: individuales: 0951+2633, galaxias: halos, materia oscura, agujeros negros primordiales.

Contents

1	Introduction	2
1.1	Motivation	2
1.2	Dark Matter	3
1.2.1	Historical context	3
1.2.2	Primordial black holes as dark matter candidates	5
1.3	Gravitational Lensing Overview	7
1.3.1	Quasar Microlensing and Primordial Black Holes	8
2	Gravitational Lensing and FBQ 0951+2635	10
2.1	Lens Equation	10
2.2	Lensing potential	11
2.3	Magnification and Distortion	12
2.4	Point lens model	14
2.5	Realistic Model for Quasar Lensing	15
2.6	Doubly Imaged Quasar FBQ 0951+2636	16
3	Methodology	17
3.1	Construction of the ODLIC	17
3.2	Magnification Maps	19
3.3	Construction of SDLICs	22
3.4	Comparison between ODLIC and SDLICs	25
4	Simulations and Results	27
4.1	First approach	27
4.2	Second approach	38
5	Conclusions	45
A	Appendix: Python programs	51
A.1	Convolution and Rotation of Magnification Maps	51
A.2	Main Program: SDLICs construction and analysis	53

Chapter 1

Introduction

1.1 Motivation

Humans have always sought to understand the cosmos and its underlying structure. Gravitational lensing has become a valuable tool in this effort, enabling a wide range of astronomical studies, from measuring the expansion of the universe and investigating the properties of distant galaxies to detecting exoplanets and exploring the early universe. One important application is studying the distribution of matter, including dark matter, which remains one of its most mysterious components. In this context, Primordial black holes (PBHs) have been proposed as potential candidates for dark matter, and their presence could be studied through microlensing effects on distant quasars.

The aim of this work is to investigate whether PBHs could constitute a significant fraction of dark matter in the universe. To achieve this, we will make use of quasar microlensing by considering different distributions of stars and primordial black holes in a given galaxy. More specifically, we will consider different contributions to the surface mass density of a given galaxy that acts as the main gravitational lens on a well-studied distant quasar, comparing the predicted extrinsic variability of the quasar (through simulations) with the observed variability through several techniques, for which we will use new and updated data. We assume that the galaxy's mass is due to smoothly distributed matter (SDM; gas or dark matter particles still undetected), a distribution of stars based on observations, and a population of PBHs with a monochromatic mass function.

Overall, this work will explore the potential contribution of PBHs to this non-local early-type galaxy acting as a gravitational lens, trying to shed light on their role in the context of dark matter.

1.2 Dark Matter

1.2.1 Historical context

Dark matter is one of the most important scientific challenges of this century. The composition of our Universe is mostly unknown, since approximately only the 5% of it corresponds to ordinary (baryonic) matter and the rest is constituted by the Dark Matter (DM) and Dark Energy (DE), see Figure 1.1. These two components are present in the current Λ CDM cosmological model to explain the origin, evolution and acceleration of the Universe [1], hence its understanding becomes crucial on our path to comprehending how the universe works. Despite all the efforts and researches made in this direction, its nature is still unknown.

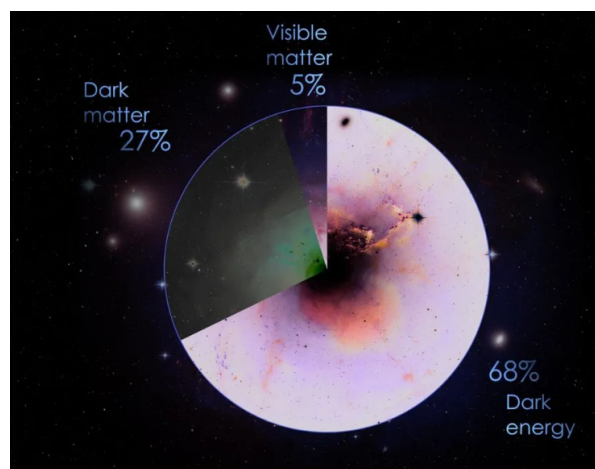


Figure 1.1: Components of the universe [2]

It has passed nearly a century since its discovery, although it was not a new concept. Angelo Secchi already claimed in 1877, from observations of nebulae, that there could be dark masses scattered in space [3]. Moreover, in his attempt to measure the Milky Way mass, considering stars as gas particles, Kelvin [4] stated that many of the stars, if not the great majority, could be dark bodies.

It was in the 30's when the idea of dark matter began to take shape as the astronomer Fritz Zwicky predicted the existence of DM by weighing the clusters [5]. He tried to analyse the distribution of galaxies within the Coma Cluster according to their radial velocities. Then, by applying the mass-to-light ratio relationship, it was possible to determine the individual luminosities of each galaxy and subsequently calculate the average mass of the cluster. Once at this point, he cross checked the result of this mass and the size of the cluster and obtained the escape velocity.

The key point was that the typical velocities of galaxies within clusters were far greater than the cluster's escape velocity. This implied that, under normal conditions, the galaxies should have drifted apart, leading to the disintegration of the cluster. However, since the clusters appeared to be stable and in equilibrium, this scenario wasn't taking place. As a result, Zwicky

proposed that there must be an unseen component, with significantly more mass than the visible matter, present within the clusters to hold the galaxies together. This marked the emergence of the concept of dark matter within the scientific community.

The other important evidence of dark matter was provided by Vera Rubin [6],[7]. She was the first to reveal a contradiction between the predicted and observed rotation curves of spiral galaxies. At that time, it was assumed that mass in a galaxy would be primarily concentrated in the luminous central bulge, much like the mass in the Solar System is concentrated in the Sun. According to Newtonian mechanics and Kepler's laws, objects further from the center of a gravitational system should rotate more slowly as gravitational force decreases with distance. Thus, the rotational velocities of stars were expected to decrease as one moves farther from the galactic center, just as planets farther from the Sun orbit more slowly.

However, Rubin's groundbreaking observations revealed a striking difference: instead of decreasing, the rotation velocity remained flat, or even increased, to distances well beyond the visible edge of the galaxies. This discrepancy, shown in Figure (1.2), challenged the existing models of galaxy dynamics.

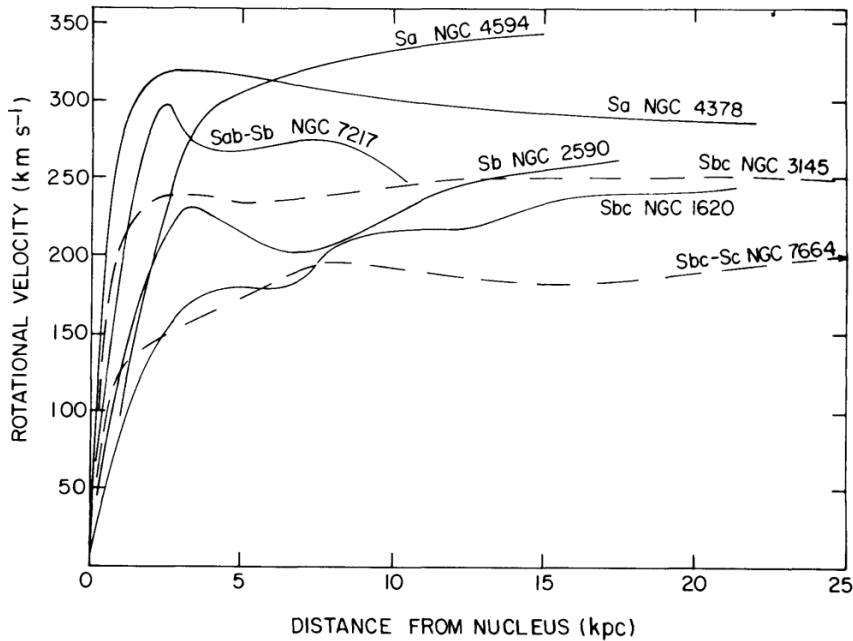


Figure 1.2: Rotational velocities for seven galaxies as a function of distance from nucleus, obtained by Rubin [6]

This unexpected behavior could only be explained if there is a large amount of unseen, "invisible" matter, which now is known as dark matter, surrounding the galaxies. This dark matter provides the additional gravitational pull needed to maintain the high rotational velocities observed at large distances from the galactic center.

1.2.2 Primordial black holes as dark matter candidates

Nowadays, the favoured hypothesis to describe the nature of dark matter is that it is collisionless. There are several candidates that have been proposed to give rise to dark matter, among which we have WIMPs (Weakly Interacting Massive Particles), MACHOs (MASSive Compact Halo Objects) such as black holes in the galaxies halos, particles arising from the supersymmetry or even neutrinos.

In this context, the discovery of gravitational waves from binary black hole mergers by the LIGO/Virgo collaboration has encouraged the community to consider the possibility that some of these BHs were of primordial origin. These hypothetical Primordial Black Holes (PBHs) would have formed just after the Big Bang, and provide an interesting explanation of the dark matter, since it does not require the introduction of any new exotic particles. The reason of this renewed interest arises from the fact that these binary black holes (BBHs) had masses higher than previously expected for black holes (BHs) of stellar origin, as well as their low spins. Therefore, this has led researchers to consider the range of masses of LIGO experiment as an important possible constituent of the dark matter in the universe.

As we have mentioned before, PBHs are those black holes formed in the early Universe through a non-stellar mechanism. Some of the pioneers in the study of PBHs were Zel'dovich and Novikov [8], who despite being limited by the lack of knowledge and observational data (which indeed led them to an erroneous discussion), found that PBHs might form from overdensities in the early Universe.

One of the main important works in this context was carried out by Stephen Hawking and Bernard Carr in the 70s [9]. Their research suggested that the mass range of PBHs could oscillate from Planck mass to several thousand times the mass of the Sun, depending on the conditions at the time of their formation. Hawking introduced the concept of Hawking radiation, suggesting that black holes emit radiation because of quantum phenomena near the event horizon, suggesting that smaller PBHs could evaporate over time due to Hawking radiation while larger ones might persist. This pioneering theory challenged the notion of black holes as entirely opaque entities, indicating instead that they could shed mass and energy over time, potentially evaporating if they don't accrete additional mass from their environment. This work marked a milestone in theoretical physics and cosmology as it laid the groundwork for future investigations and led to the possibility of PBHs explaining DM.

Actually, PBHs satisfy all of the necessary requirements to be a good dark matter candidate since they are cold, non-baryonic (as they were originated before nucleosynthesis and can be produced in adequate quantities). In addition, despite emitting Hawking radiation, PBHs are cosmologically stable (their lifetime is longer than the age of the Universe) if their initial mass is

greater than $\sim 10^{15}$ g [10]. Moreover, unlike most other DM candidates (WIMPs, axions, sterile neutrinos,...) PBHs are not a new exotic particle (which is undoubtedly an advantage) but its existence is a rather natural consequence of several inflationary scenarios (although they hence require "Beyond the Standard Model" physics).

It should be noted that, revisiting the list of black holes detected by gravitational waves [11], a significant number of them corresponds to the range of (5-20) M_{\odot} , hence we have considered in the analysis a value of $10 M_{\odot}$. Despite BHs of $\sim 10M_{\odot}$ can be of stellar origin (consequence of massive stars evolution), stellar black holes (SBHs) can only contribute with a few per cent of the total mass in stars. As a consequence, we have considered PBH fractions of microlenses above 10% to distinguish between PBHs with $\sim 10M_{\odot}$ and other with similar mass. Note that we do not have this problem for the other PBHs mass analysed (10^{-3} and $0.1 M_{\odot}$), as they can't be of stellar origin.

The constraints on the fraction of DM in the form of PBHs with mass M , f_{pbh} , are summarized in Figure 1.3:

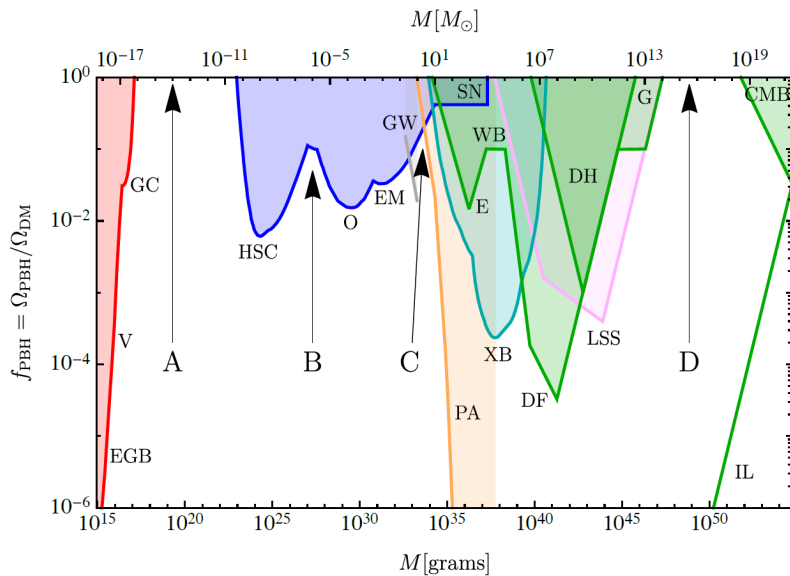


Figure 1.3: Constraints on the fraction of DM in the form of PBHs, f_{pbh} , with mass M , coming from evaporations (red), lensing (blue), gravitational waves (GW) (gray), dynamical effects (green), accretion (light blue), CMB distortions (orange) and large-scale structure (purple), from [12].

From Figure 1.3, there are four mass windows (A, B, C, D) in which PBHs could have an appreciable density. Nevertheless, it should be noted that these constraints correspond to different redshifts. Furthermore, the constraints established through microlensing studies in Figure 1.3 for the mass range (10^{-3} - $0.1 M_{\odot}$) correspond to observations from local galaxies (Milky Way and Magellanic Clouds) whereas this work focuses on observations of a non-local early-type galaxy. However, apart from being candidate to DM, the importance of PBHs is self-evident since it might be a possible solution for other astrophysical open questions; for instance, they could be the precursors of the supermassive black holes found at the cores of galaxies or the intermediate-mass black holes that might reside at the centers of dwarf galaxies [13].

1.3 Gravitational Lensing Overview

Cosmology is continually evolving due to new discoveries in a wide variety of fields of modern physics and astrophysics. Some of these discoveries are achieved through the gravitational lensing effect, which provides detailed insights into the composition of galaxies and their peculiar velocities.

Gravitational lensing is a phenomenon where the presence of a massive object, such as a galaxy or a cluster of galaxies, bends and magnifies the light from a background source, such as a star or quasar. This effect, that can generate multiple images of the background source, is a natural consequence of Einstein's General Theory of Relativity, according to which light follows geodesics arising from the space-time curvature (caused by a given mass), much like how a lens bends light in optics. However, this idea was conceived before Einstein. Isaac Newton already speculated about the gravitational influence on light in 1704 in his book 'Opticks' [14], where he proposed that light consists of particles that would be influenced by gravity, much like any other matter. Newton hypothesized that light particles passing near a massive object would be deflected by its gravitational pull, although he did not provide a mathematical framework for this effect. Later in 1784, Henry Cavendish (motivated by John Mitchell ideas related to the reduction in the light speed by effect of gravity) calculated the Newtonian deflection of light for the first time, although he did not publish his results [15]. It wasn't until the beginning of the XIXth century when these calculations were published in an official document by Johann Soldner (1801) a German mathematician who deduced that a light ray near the solar limb would be deflected by an angle of $\Delta\phi = 0.84$ arcsec [16].

In 1911, more than a century later, Albert Einstein studied the impact of gravity on light in his work "On the Influence of Gravity on the Propagation of Light." [17]. Nevertheless the first value he obtained for the deflection angle was the same one Soldner calculated using Newton mechanics, as at this time, the General Theory of Relativity had not yet been fully formulated. In his paper, Einstein determined the deflection angle $\tilde{\alpha} = 2GM/c^2R = 0.83$ arcseconds for a light ray skimming the sun, where M and R are the mass and radius of the sun, and c and G are the speed of light and the gravitational constant, respectively. Despite the efforts made by Einstein and several researchers to study experimentally the deflection effect, the opposition from the scientific community as well as external conditions (in particular the World War I), delayed the measurement of the deflection angle at the solar limb for a few years, which paradoxically worked in Einstein's favor since the value he obtained was wrong. It was with the completion of the General Theory of Relativity when he derived the correct deflection angle $\tilde{\alpha} = 1.74$ arcsec [18].

According to this theory, gravity is not just a force between masses but rather a result of the warping of space-time by mass and energy. Light, which always travels along the shortest path in space-time, follows geodesic lines (in a curved space-time, geodesic lines are the paths that

are as straight as possible under the circumstances, similar to straight lines in flat space-time). As light rays travel along these geodesic lines, they bend towards the mass that is causing the curvature of space-time, hence altering the path light takes. This was verified by Arthur Eddington and his group during a solar eclipse in 1919 that indeed was the second observational confirmation of General Relativity and reinforced Einstein's theory, which eventually changed our understanding of how the universe works.

Nevertheless, it took more than half a century to observationally confirm this phenomenon in other environments. In the following decades, gravitational lensing was rarely the focus of research papers. In 1924, Chwolson proposed the concept of a "fictitious double star" and described the symmetrical case of a star directly behind another star, resulting in a circular image [19]. Einstein also carried out in 1936 the same discussion about the appearance of a "luminous circle" for perfect alignment between source and lens, and two magnified images for slightly misaligned positions. This configuration is actually known as an "Einstein-ring". In this context, Fritz Zwicky [5], [20] suggested in 1937 that galaxies, or "extragalactic nebulae," are much more likely to be gravitationally lensed than stars and proposed using the gravitational lens effect as a "natural telescope".

However, the field became specially important in the 60s, with the discovery of quasars and the development of several independent theoretical studies which demonstrated the potential of lensing for astronomy. For instance, Sjur Refsdal [21] showed how the gravitational lens effect could be used to determine Hubble's constant by measuring the time delay between two lensed images. Moreover, gravitational lensing received an important boost in 1979, when the first double quasar was discovered and confirmed as a true gravitational lens by Walsh, Carswell, and Weymann [22].

Since then, the field of gravitational lensing has been continuously growing and a wide variety of phenomena have been discovered. Among these, the most notable are weak lensing (when the gravitational lens only produces a small shift in the angular position of the source), strong lensing (when it produces multiple images or a ring of a background source, where the typical separation between images for a galaxy-quasar system is $\sim 1''$) and microlensing (when stars within the lensing galaxy can act as micro-lenses, generating images with separations of the order of $\sim 10^{-6}''$, i.e, a microarcsecond).

1.3.1 Quasar Microlensing and Primordial Black Holes

Some galaxies have a significant activity in their central regions, where accretion towards a supermassive black hole is most likely responsible for this activity: very high luminosity, strong variability, etc. These central regions are called Active Galactic Nuclei (AGN). Quasars are very bright and distant AGN. They emit light across the entire electromagnetic spectrum, from radio

waves to gamma rays, and exhibit variability on nearly all timescales [23]. At the center of a quasar is a Super-Massive Black Hole (SMBH) surrounded by an accretion disk, a few light-days in size, which is responsible for part of the continuum emission. Additionally, a region extending hundreds of light-days contains clouds of ionized gas that produce broad emission lines. The relatively small size of the accretion disk makes it susceptible to gravitational microlensing (ML), hence among all the phenomena mentioned in the previous section, we are particularly interested in quasar microlensing.

Gravitational microlensing (ML) occurs when a compact object, such as a star, black hole, brown dwarf, or planet, passes in front of a distant light source, causing the light to bend and create additional images. These "microlenses" produce multiple, closely spaced images of the background source, although the separations are usually too small to be resolved by current telescopes. Instead, microlensing events are typically observed as changes in the brightness of the source over time.

Quasar microlensing combines these phenomena, utilizing the variability and brightness of quasars to study the microlensing effect. When a quasar's light is magnified by an intervening galaxy, each of these stars (or other compact objects, like black holes, brown dwarfs, or planets) which conform the galaxy, acts as a "compact lens" or "microlens" and produces at least one new image of the source [24]. This creates numerous micro-images that blend into the observed macro-image. Despite their very small separations, which are on the order of micro-arcseconds and unresolvable with present technology, the impact of microlensing on the total flux can be monitored through light curves which can be studied, and, as we will see, might reveal important information about the mass distribution and abundance of compact objects present in the lens galaxies.

Chapter 2

Gravitational Lensing and FBQ 0951+2635

2.1 Lens Equation

Before going any further, it is useful to explain the basics of gravitational lensing, so that we can understand the underlying physics of quasar microlensing, crucial to achieving our goal. As we already mentioned before, gravitational lensing is based on light deflection caused by massive objects bending spacetime. It is useful to make an initial approximation, assuming a thin lens and a weak gravitational potential, i.e, a lens whose Newtonian gravitational potential ψ is much smaller than c^2 , $|\psi| \ll c^2$, and that its thickness is small when compared to the total dimensions of the optical system. It should be noted that this approximation is valid in most scenarios, since the physical size of the lens is generally much smaller compared to the distances between observer, lens and source. Therefore, in this approximation, the lens is well approximated by a planar distribution of matter which is known as the lens plane. Note that the sources are also assumed to lie on the source plane.

Thus, the distribution of the lensing matter in this context is completely characterised by the surface density Σ , defined as the projection of the three dimensional density ρ along the line of sight onto the lens plane. It can be expressed as:

$$\Sigma(\vec{\xi}) = \int \rho(\vec{\xi}, z) dz \quad (2.1)$$

where $\vec{\xi}$ is a two-dimensional vector in the lens plane.

Given a distribution of mass elements on the lens plane $\Sigma(\vec{\xi}) d^2 \xi$, it can be shown that the total deflection angle in this approximation is obtained by summing their contributions:

$$\vec{\alpha}(\vec{\xi}) = \frac{4G}{c^2} \int \frac{(\vec{\xi} - \vec{\xi}') \Sigma(\vec{\xi}')}{|\vec{\xi} - \vec{\xi}'|^2} d^2 \xi' \quad (2.2)$$

We can illustrate a gravitational lens system in Figure (2.1), assuming a point source S and L to be the center of the mass distribution, in which the deflexion in $\vec{\xi}$ is due to the whole mass being concentrated in points $\vec{\xi}'$, and light rays emitted by the source are deflected producing (at least)

two images (S_1 and S_2). In this figure, we can see the different angular diameter distances D_L , D_S , D_{LS} as well as the relevant angles.

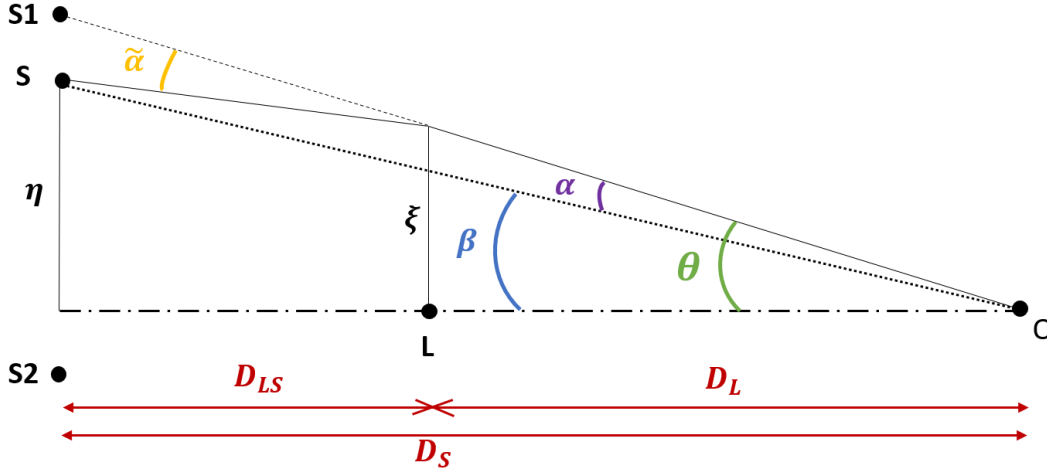


Figure 2.1: Gravitational lens setup for a point source S and a lens L located between source and observer O , producing two images S_1 and S_2 . Figure made by the author.

The source S in Figure 2.1 is at an angular position $\vec{\beta}$ whereas $\vec{\alpha}$ is the deflection angle of the light ray coming from S (as a consequence of deflection, the observer perceives the light as it was emitted at the angular position $\vec{\theta}$). In general, the angles $\vec{\theta}$, $\vec{\beta}$, $\vec{\alpha}$, $\vec{\alpha}$ are not coplanar, hence they have to be expressed in its vector form, where each angle has two components in the plane of the sky [25].

Therefore, from Figure (2.1) and assuming that $\vec{\theta}$, $\vec{\beta}$, $\vec{\alpha}$ are small, we can obtain the following relation:

$$\vec{\theta}D_S = \vec{\beta}D_S + \vec{\alpha}D_{LS} \quad (2.3)$$

In addition, we could define the reduced deflection angle $\vec{\alpha}$ as:

$$\vec{\alpha}(\vec{\theta}) = \frac{D_{LS}}{D_S} \vec{\alpha}(\vec{\theta}),$$

hence Equation (2.3) is reduced to

$$\vec{\beta} = \vec{\theta} - \vec{\alpha}(\vec{\theta}) \quad (2.4)$$

which is known as the lens equation.

2.2 Lensing potential

The deflection angle can be expressed as the gradient of an effective two-dimensional scalar potential ψ ($\vec{\nabla}_\theta \psi = \vec{\alpha}$), known as the effective lensing potential, which is obtained by projecting and rescaling the three-dimensional Newtonian potential on the lens plane [18]:

$$\psi(\vec{\theta}) = \frac{D_{\text{LS}}}{D_{\text{L}}D_{\text{S}}} \frac{2}{c^2} \int \Phi(\vec{r}) dz$$

where $\Phi(\vec{r})$ is the Newtonian potential of the lens.

Additionally, the lensing potential satisfies an important property, as the Laplacian of ψ is twice the convergence:

$$\Delta_{\vec{x}}\psi(\vec{x}) = 2\kappa(\vec{x}).$$

which is defined as a dimensionless surface density

$$\kappa(\vec{x}) \equiv \frac{\Sigma(\vec{x})}{\Sigma_{\text{cr}}} \quad \text{with} \quad \Sigma_{\text{cr}} = \frac{c^2}{4\pi G} \frac{D_{\text{S}}}{D_{\text{L}}D_{\text{LS}}},$$

where Σ_{cr} is known as the critical surface density, a quantity that defines the lens system and depends on the angular diameter distances.

2.3 Magnification and Distortion

Light bundles are typically deflected differently. As a consequence the shape of the sources are distorted, and this becomes more evident when the source has no negligible apparent size. Ideally, the shape of the images can be determined by solving the lens equation for all points within the extended source. In particular, if the source is much smaller than the angular scale over which the physical properties of the lens vary, the relation between source and image positions can be locally linearized, hence the image distortion can be described by the Jacobian matrix [18]:

$$\mathcal{A} = \frac{\partial \vec{\beta}}{\partial \vec{\theta}} = \left(\delta_{ij} - \frac{\partial \alpha_i(\vec{\theta})}{\partial \theta_j} \right) = \left(\delta_{ij} - \frac{\partial^2 \psi(\vec{\theta})}{\partial \theta_i \partial \theta_j} \right) \quad (2.5)$$

We can define the components of the external shear γ as

$$\begin{aligned} \gamma_1(\vec{\theta}) &= \frac{1}{2} (\psi_{11} - \psi_{22}) = \gamma \cos(2\varphi) \\ \gamma_2(\vec{\theta}) &= \psi_{12} = \psi_{21} = \gamma \sin(2\varphi) \end{aligned} \quad (2.6)$$

where the angle φ represents the orientation of the shear-inducing tidal force with respect to the coordinate system. The shear quantifies the projection of the gravitational tidal field (the gradient of the gravitational force), hence describes distortions of background sources.

Taking this into account, it can be shown [15] that the Jacobian matrix can be expressed in terms of convergence and shear:

$$\mathcal{A} = \begin{pmatrix} 1 - \kappa - \gamma_1 & -\gamma_2 \\ -\gamma_2 & 1 - \kappa + \gamma_1 \end{pmatrix} = (1 - \kappa) \begin{pmatrix} 1 & 0 \\ 0 & 1 \end{pmatrix} - \gamma \begin{pmatrix} \cos 2\varphi & \sin 2\varphi \\ \sin 2\varphi & -\cos 2\varphi \end{pmatrix} \quad (2.7)$$

Note that the distortion induced by the convergence is isotropic as images are rescaled equally in all directions, while the shear distorts the intrinsic shape of the source along a specific direction (where $\gamma = (\gamma_1^2 + \gamma_2^2)^{1/2}$ represents the magnitude of the shear and φ specifies its orientation). This is shown in Figure (2.2).

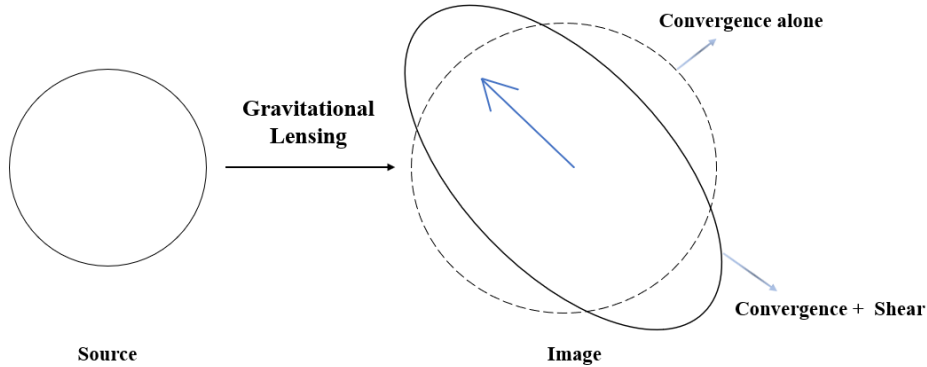


Figure 2.2: Convergence and shear on a circular source. Convergence modifies the image isotropically while shear deforms it to an ellipse. Figure made by the author.

Furthermore, apart from light distortion, another characteristic phenomena of gravitational lensing is magnification. As we can see from Equation (2.4), a solid angle element $\delta\beta^2$ is transformed into the solid angle $\delta\theta^2$. Given that the surface brightness is conserved (ensured by the Liouville theorem and the absence of emission and absorption of photons in gravitational light deflection [15]), the change of the solid angle under which the source is seen results in a change in the flux received from the source, either increasing (magnifying) or decreasing (demagnifying) it.

Given Equation (2.5), magnification is quantified by the inverse of the Jacobian matrix determinant

$$\mu = \frac{1}{\det \mathcal{A}} = \frac{1}{(1 - \kappa)^2 - \gamma^2} \quad (2.8)$$

Note that, there are relevant locations in Equation (2.8), for which $\det \mathcal{A} = 0$, hence the magnification is formally infinite $\mu \rightarrow \infty$. These locations are known as critical curves in the lens plane, and the corresponding ones in the source plane are called caustics (i.e, the sources that produce images around the critical lines are located along the caustics). As it was mentioned previously, if the lens is strong, multiple images can be formed of the same source. The number of these images depends on the position of the source with respect to the caustics as when the source track crosses a caustic, a pair of highly magnified microimages either appear newly or merge and disappear.

2.4 Point lens model

We analyse first the simplest lens model in order to derive easily different properties of the lens system. In this context, it can be proved that the deflection angle can be expressed only in one dimension for axially symmetric lenses, since all light rays from the source to the observer must lie in the plane spanned by the center of the lens, the source and the observer [15]. Therefore, considering a point lens of mass M , it can be shown that the corresponding deflection angle of Equation (2.2) is simplified to:

$$\tilde{\alpha} = \frac{4GM}{c^2 D_L \theta} \quad (2.9)$$

Furthermore, with the previous definition of Σ_{cr} , the deflection angle for this mass distribution can be expressed as

$$\tilde{\alpha}(\theta) = \frac{\Sigma}{\Sigma_{\text{cr}}} \theta$$

We can replace this deflection angle into Equation (2.4), which is reduced to,

$$\beta(\theta) = \theta - \frac{D_{\text{LS}}}{D_L D_S} \frac{4GM}{c^2 \theta}$$

At this stage, it is useful to introduce the Einstein radius, which is defined as [15]:

$$R_E = \sqrt{\frac{4GM}{c^2} \frac{D_{\text{LS}}}{D_L D_S}} \quad (2.10)$$

It is an important magnitude in gravitational lensing that defines the angular scale in a lens system. In particular, it sets a typical scale for separation between multiple images. For a massive galaxy with a mass of $M \sim 10^{12} M_\odot$ at a redshift of $z \sim 0.5$ and a source quasar at $z \sim 2$, the Einstein radius is of a few arcoseconds. Stars within the lens galaxy also produce gravitational lensing effects, and the corresponding separation between images would be only of a few microarcseconds ($10^{12} M_\odot \rightarrow 1 M_\odot$). We are particularly interested in these microlensing effects. The Einstein radius is also defined as the angular radius of the case in which the source lies exactly behind the lens ($\beta = 0$), where we have a ring-like image as a consequence of the symmetry, known as the Einstein ring, see Figures 3.4, 3.5

However, despite the fact that a point lens model is useful to understand basic observations in strong gravitational lensing, realistic lens models are required to accurately describe all observational data for a galaxy-quasar lens system (see Sect. 2.5).



Figure 2.3: JWST-ER1 Einstein Ring [26]



Figure 2.4: Idealized Einstein ring, digital artwork by IncrediVFX

2.5 Realistic Model for Quasar Lensing

The point mass model explained before provides a fundamental understanding of gravitational lensing, being an idealization that assumes the lens is a single and infinitesimally small object. Although this simple model has proved to be useful to introduce the fundamental concepts of gravitational lensing, real lensing galaxies are not point-like but extended objects with complex mass distributions. Nevertheless, lens mass models must be characterized by a number of parameters less than or equal to the number of observational constraints, so a realistic model incorporates an observationally-motivated rough description of the main lens galaxy along with the gravitational effects by secondary deflectors. In this context, an isothermal ellipsoid has a density proportional to r^{-2} and it is consistent with the flat rotation curves observed in the Milky Way and other spiral galaxies (see Figure 1.2). However, deviations from isothermality are possible, and thus, the main lens galaxy is usually described as a singular power-law ellipsoid (SPLE) whose density (convergence) is given by the dimensionless surface [27]:

$$\kappa_{\text{gal}}(x, y) = \frac{b^{2-\alpha}}{2(x^2 + y^2/q^2)^{1-\alpha/2}}$$

where $M(\alpha) \sim r^\alpha$ with $\alpha = 1$ for the isothermal case, $\alpha < 1$ steeper than isothermal and $\alpha > 1$ if shallower than isothermal. Here, b is the mass scale in arcseconds and q is the projected axis ratio. Nevertheless, a few main lens galaxies are isolated, and they usually have neighbours or are embedded in halos of groups or clusters. These environments can play a role to explain the observations of the lens system. In addition to the perturbations of objects or structures near the main lens galaxy, objects or structures along the line of sight also perturb the lensing potential [28]:

$$\psi_{\text{ext}} \approx \frac{r^2}{2} [\kappa_{\text{ext}} + \gamma_{\text{ext}} \cos 2(\theta - \theta_{\gamma_{\text{ext}}})], \quad (2.11)$$

where, κ_{ext} is the external convergence (a uniform mass sheet with surface density $\Sigma_{\text{ext}} = \kappa_{\text{ext}} \Sigma_{\text{cr}}$), γ_{ext} is the external shear strength and $\theta_{\gamma_{\text{ext}}}$ represents the direction of the external tidal shear

(pointing towards the mass concentration producing it).

2.6 Doubly Imaged Quasar FBQ 0951+2636

The gravitational lens system FBQ 0951+2635 was discovered by [29]. The lensed quasar is located at a redshift $z_{\text{qso}} = 1.246$ [30] and the early-type lensing galaxy has a redshift $z_{\text{gal}} = 0.260$ [31]. The brightest optical image is denoted by the letter A, and the faintest optical image is denoted by B. The relative astrometry of the image B and the main lens galaxy (with respect to A), and the light distribution of the galaxy were also derived from new IR HST observations [30]. Additionally, the optical light curves in the period 1999-2001 yielded a time delay of $16 \pm 2d$ (see [30]). The discovery by [31] also reported the flux ratio $B/A = 0.21 \pm 0.03$ at 8.4 GHz. Radio fluxes are expected to be unaffected by microlensing (large source) and dust extinction, and taking into account the short delay of, about two weeks, the radio flux ratio is a good proxy of the microlens magnification ratio (due to the galaxy as a whole).

Using the observational constraints of the system in the previous paragraph, as well as a standard flat Λ CDM cosmology with $M = 0.3M_{\odot}$ and $\Omega_{\Lambda} = 0.7$, [32] obtained a lens mass solution based on a realistic lens model consisting of a SPLE and external shear (ES).

This solution allows us to obtain the total convergence (κ), the total shear strength (γ) and the shear direction (θ_{γ}) at the positions of both quasar images (A and B; see the second row in Table 2.1).

Approach	κ_A	γ_A	θ_{γ_A}	κ_B	γ_B	θ_{γ_B}
1	0.2786	0.3800	36.28	1.1938	1.3517	49.91
2	0.4012	0.3154	36.28	1.1608	1.1219	49.91

Table 2.1: Values for the convergence κ and shear γ as well as for the shear angles θ_{γ} , which are in degrees east of north, for both images.

In a second approach it is considered a more robust time delay of 13.3 ± 1.7 d, which relies on optical light curves in the periods 1999–2001 and, 2008-2023, (covering 19 years of observations).

In addition, [33] performed a spectroscopy survey of galaxies along the sightline, putting constraints on the external convergence κ_{ext} . Using the new time delay and the lower limit on $\kappa_{\text{ext}} (= 0.17)$ as a reference value, one can demonstrate that Ruiz-Hinojosa's lens solution is still usable as an "effective" solution. As the effective model (SPLE+ES) does not incorporate the external convergence, galaxy's mass scale and the external shear strength are overestimated with respect to their real values b and γ_{ext} . Thus, the effective solution includes the values of $b^* = b/(1 - \kappa_{\text{ext}})$ and $\gamma_{\text{ext}}^* = \gamma_{\text{ext}}/(1 - \kappa_{\text{ext}})$. It is also easy to show that the real convergence is $\kappa = \kappa_{\text{gal}} + \kappa_{\text{ext}}$, where $\kappa_{\text{gal}} = (1 - \kappa_{\text{ext}})\kappa^*$ and κ^* is the effective convergence. Similarly, the real shear strength is $\gamma = (1 - \kappa_{\text{ext}})\gamma^*$, with γ^* being the effective shear strength (see the third row in Table 2.1).

Chapter 3

Methodology

3.1 Construction of the ODLC

The observed difference light curve (ODLC) is built from GLENDAMA+ light curves of FBQ 0951+2635, mainly consisting of optical magnitudes provided by observations with the Liverpool Telescope (GLENDAMA project) and the Kaj Strand Telescope at the United States Naval Observatory Flasftaff station (see Figure 3.1). The brightness records cover the period 2008-2023 (updated on December 1, 2023).

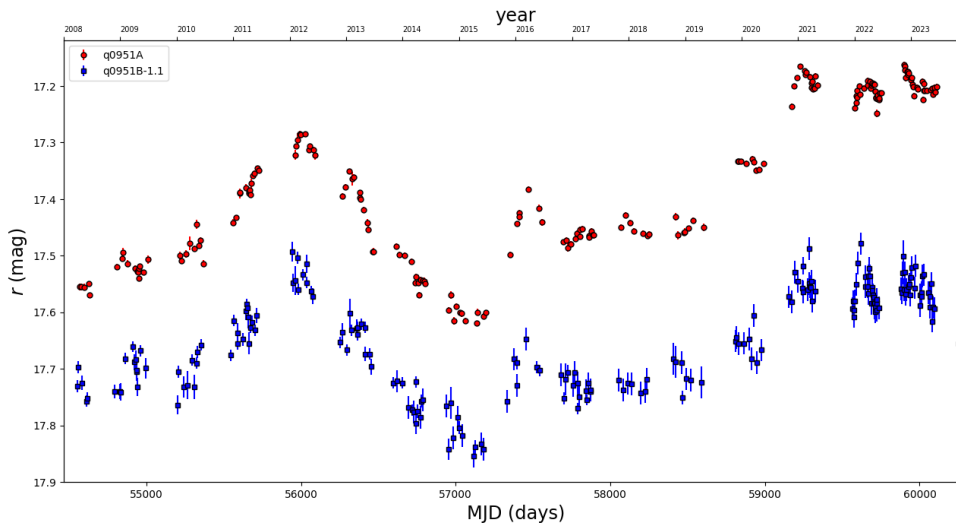


Figure 3.1: Observed light curves for A and B images of quasar FBQ 0951+2635 for the first approach, with time delay removed and a displacement of 1.1 in B to see more clear both curves.

Thus, the ODLC informs us on the extrinsic (microlensing) variability of the quasar images, since quasar intrinsic variations are removed as can be seen next. The flux of the quasar image B at time t is given by

$$F_B(t) = F_I(t)\epsilon_B\mu_B(t)$$

where F_I is the intrinsic quasar flux, ϵ_B is the dust extinction factor, and μ_B is the lens magnification. This lens magnification might vary over time as the source quasar moves across the sky. Additionally, taking into account the time delay between the two quasar images (dt), we can write:

$$F_A(t - dt) = F_I(t)\epsilon_A\mu_A(t)$$

Furthermore, if we subtract the two previous expressions and use magnitudes instead of fluxes,

$$B(t) - A(t - dt) = -2.5 \log \left[\frac{F_B(t)}{F_A(t - dt)} \right] = -2.5 \log \left[\frac{\epsilon_B \mu_B(t)}{\epsilon_A \mu_A(t)} \right] \quad (3.1)$$

as F_I is conveniently removed. By subtracting now the average (mean) level $\langle B(t) - A(t - dt) \rangle$, it is possible to remove dust extinction effects. Therefore,

$$B(t) - A(t - dt) - \langle B(t) - A(t - dt) \rangle = -2.5 \left\{ \log \left[\frac{\mu_B(t)}{\mu_A(t)} \right] - \langle \log \left[\frac{\mu_B(t)}{\mu_A(t)} \right] \rangle \right\} \quad (3.2)$$

The observational data (GLEDAMA+ light curves) has allowed us to construct the ODLC (see the left side of Equation (3.2)), which have been compared with synthetic difference light curves (SDLCs) from simulations (magnification maps; see the right side of the Equation (3.2)).

Moreover, it can be seen from Equation (3.2) that the ODLC depends on the time delay dt . Once at this stage, we have considered two different approaches (see Section 2.6) involving two time delays. For the first one ($dt = 16$ d), we have obtained the ODLC in Figure 3.2.

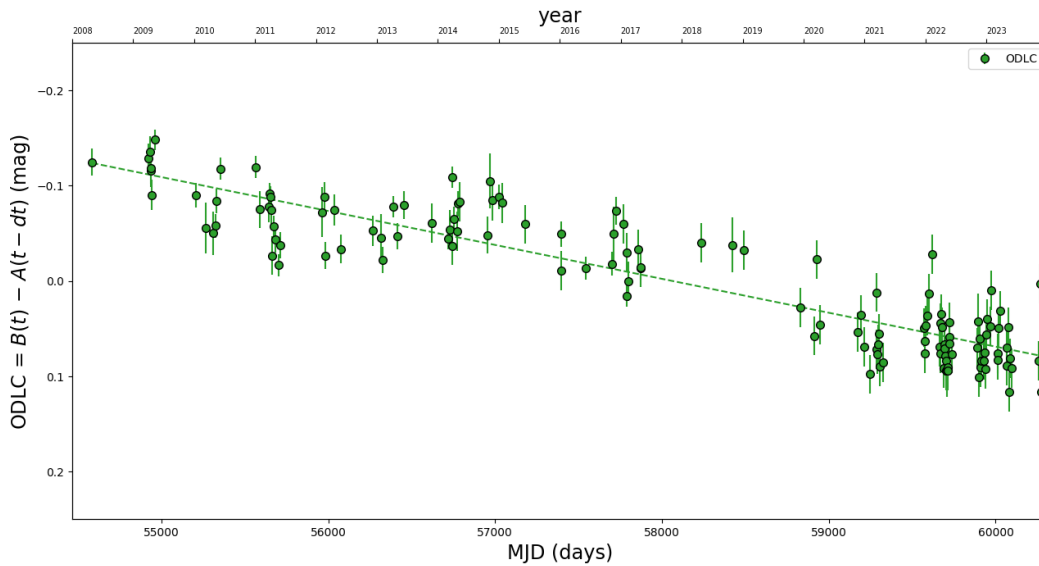


Figure 3.2: Observed difference light curve of quasar FBQ 0951+2635 for the first approach.

The ODLC for the second one ($dt = 13.3$ d) is very similar to that for the first one, hence it is not worthwhile to show such difference curve. Nevertheless, we show below both ODCLs:

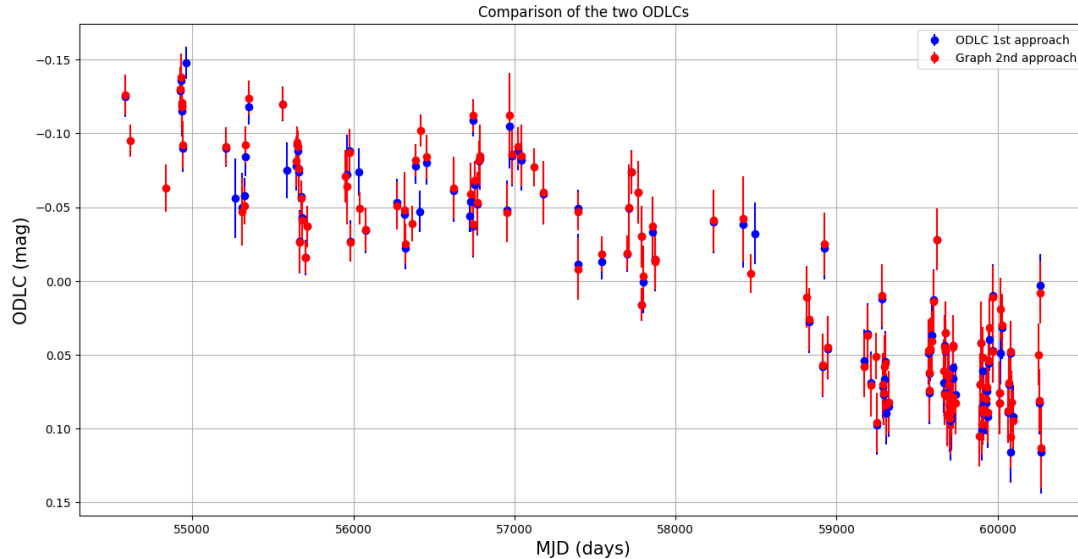


Figure 3.3: ODLCs generated with the first and second approaches

From Figure 3.3, it can be seen as we anticipated, that there is not an important difference between both ODLCs. Furthermore, we have calculated the mean of the differences, obtaining a value of $\mu_{\text{diff}} = 0.003$, which is a very low value. Additionally, the correlation coefficient between both data has been also determined, obtaining a value of $R^2 = 0.996$, which clearly indicates a very high degree of similarity between the two sets of data.

3.2 Magnification Maps

Once we already have the ODLC, the next step is the construction of synthetic difference light curves (SDLCs) to be compared with the observed difference light curve. They will be obtained from trajectories in magnification maps for each image, which have been made with a fortran code that calculates magnification maps corresponding to some amount of smoothly distributed mass, and two populations of microlenses (stars and PBHs; see [34] for a simpler version addressing a single population of microlenses).

In the first approach to describe the lens system, the convergence is exclusively due to the lens galaxy ($\kappa_{\text{ext}} = 0$), and it can be decomposed into three contributions: smoothly distributed matter in the galaxy halo (κ_{sdm}), stars (κ_{star}) and PBHs (κ_{pbh}). Thus, we define the two independent parameters $f_{\text{sdm}} = \kappa_{\text{sdm}}/\kappa$ (SDM Fraction) and $F_{\text{pbh}} = \frac{\kappa_{\text{pbh}}}{\kappa_{\text{star}} + \kappa_{\text{pbh}}}$ (PBH Fraction of microlenses). Once we set f_{sdm} and the PBH fraction, we get that $f_{\text{pbh}} = F_{\text{pbh}}(1 - f_{\text{sdm}})$, and the star fraction is given by $f_{\text{star}} = 1 - F_{\text{pbh}}(1 - f_{\text{sdm}}) - f_{\text{sdm}}$.

Therefore, we have considered three values of f_{sdm} (0.1, 0.5 and 0.9) and three values of F_{pbh} (0.1, 0.5 and 0.9). The total possible mass distributions are displayed in Table 3.1:

Fraction	#1	#2	#3	#4	#5	#6	#7	#8	#9
f_{sdm}	0.1	0.1	0.1	0.5	0.5	0.5	0.9	0.9	0.9
F_{pbh}	0.1	0.5	0.9	0.1	0.5	0.9	0.1	0.5	0.9
f_{pbh}	0.09	0.45	0.81	0.05	0.25	0.45	0.01	0.05	0.09
f_{star}	0.81	0.45	0.09	0.45	0.25	0.05	0.09	0.05	0.01

 Table 3.1: Combinations for the parameters f_{sdm} , f_{pbh} and f_{star} .

In the second approach, the SDM fraction includes both the contribution from the lensing galaxy (κ_{sdmgal}), and that from matter halos near the galaxy and along the line of sight, which act as secondary deflectors (κ_{ext}). More specifically, $f_{\text{sdm}} = \kappa_{\text{ext}}/\kappa + f_{\text{sdmgal}}(1 - \kappa_{\text{ext}}/\kappa)$, and each value we use for $f_{\text{sdmgal}} = \kappa_{\text{sdmgal}}/\kappa_{\text{gal}}$, i.e, 0.1, 0.5, 0.9, leads to $f_{\text{sdm}}(A) \neq f_{\text{sdm}}(B)$. This fact is shown in the following scheme:

$$\begin{aligned}
 f_{\text{sdmgal}} = 0.1 &\rightarrow f_{\text{sdm}}(A) = 0.48 \quad \text{and} \quad f_{\text{sdm}}(B) = 0.23 \\
 f_{\text{sdmgal}} = 0.5 &\rightarrow f_{\text{sdm}}(A) = 0.71 \quad \text{and} \quad f_{\text{sdm}}(B) = 0.57 \\
 f_{\text{sdmgal}} = 0.9 &\rightarrow f_{\text{sdm}}(A) = 0.94 \quad \text{and} \quad f_{\text{sdm}}(B) = 0.91
 \end{aligned}$$

Given the values of f_{sdmgal} and F_{pbh} , we set the mass fraction of the galaxy in PBHs, $f_{\text{pbhgal}} = F_{\text{pbh}}(1 - f_{\text{sdmgal}})$, and in stars $f_{\text{stargal}} = 1 - F_{\text{pbh}}(1 - f_{\text{sdmgal}}) - f_{\text{sdmgal}}$. As in the first approach, we take three values of F_{pbh} (0.1, 0.5 and 0.9).

After introducing the mass distributions, it is convenient to discuss the microlenses mass. A power law is usually assumed for the mass function of stars, where $N(M) dM \propto M^{-\alpha} dM$. denotes the number of stars with masses between M and $M+dM$ ($M_1 < M < M_2$) and $r = M_2/M_1$ is the maximum - to - minimum mass ratio. For example, [35] used a Salpeter mass function ($\alpha = 2.35$) with $r = 100$ for stars in the bulge of a local spiral galaxy, while [36] used a Kroupa mass function ($\alpha = 1, 3$) with $r = 50$ for stars in non-local, early-type galaxies. The new microlensing simulator (modified version of that in [34]) considers both α values and $r = 50$, although we have focused on $\alpha = 1.3$ (e.g, [37], [38]; both inspired by the mass function of Gould [39]). Although magnification maps are obtained for an arbitrary mean star mass (it is not necessary to set its value), we have adopted a typical mean mass $M_{\text{star}} = 0.3M_{\odot}$. Regarding the mass of the PBHs, we have assumed a monochromatic mass function (all PBHs equal mass) and considered three different values of $r_{\text{pbh}} = \log(M_{\text{pbh}}/M_{\text{star}})$. These values are $r_{\text{pbh}} = -2.5$ ($M_{\text{pbh}} \approx 10^{-3}M_{\odot}$; giant-planet-like PBHs), $r_{\text{pbh}} = -0.5$ ($M_{\text{pbh}} \approx 0.1M_{\odot}$; red-dwarf-like PBHs) and $r_{\text{pbh}} = 1.5$ ($M_{\text{pbh}} \approx 10M_{\odot}$; SBH-like PBHs).

Using 9 distributions of mass (see, e.g. Table 3.1 for the first approach) and 3 values of the PBH mass, we have generated 27 magnification maps with a given size and resolution for each image in the two approaches. Following [38], we built maps of 40 Einstein radii on each side, where Einstein radius is given by $R_E(M_{\text{star}}) = \left[\left(\frac{4GM_{\text{star}}}{c^2} \right) \left(\frac{D_s D_{Ls}}{D_L} \right) \right]^{1/2} = 3.76 \times 10^{16} \text{cm}$. These

maps contain 8000×8000 pixels.

We show below, the magnification maps corresponding to the first approach for the scenario 010125 ($f_{\text{sdm}} = 0.1$, $F_{\text{pbh}} = 0.1$, $r_{\text{pbh}} = -2.5$), for both images.

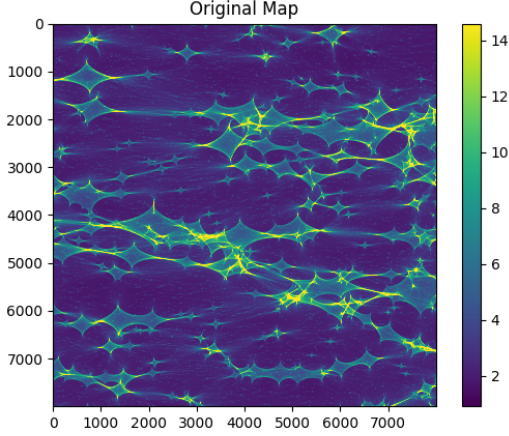


Figure 3.4: Magnification map for image A in the first approach

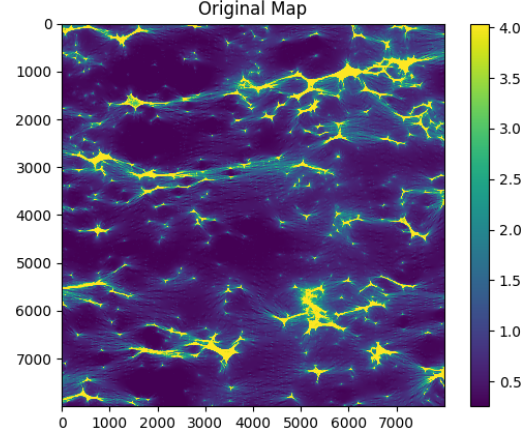


Figure 3.5: Magnification map for image B in the first approach

Since the source has a finite size, one must convolve the 27 initial maps with a Gaussian brightness profile $I(R) \propto \exp(-R^2/2R_S^2)$ that is characterised by a relative source radius $r_S = R_S/R_E(M_{\text{star}})$. In this work, we consider the two values of r_s that were measured by [38]: $r_s = 0.605$ (fit of optical data) and $r_s = 0.276$ (joint fit of near IR and optical data), as well as a smaller value of $r_s = 0.1$ for comparison purposes (to check the feasibility of a more compact source).

As a summary, we finally produce 81 ($9 \times 3 \times 3$) magnification maps for each image and approach, using the parameters in Table 2.1.

We also note that the shear points towards the mass that produces it, and this radial direction forms an angle θ_γ with the celestial north. The magnification map of an image is thus constructed using a coordinate system in which the two axes coincide with the radial and tangential directions. Therefore, the map of one of the two images must be conveniently rotated to analyse a given source trajectory across the sky in the maps of both images (e.g Figure 2 of [40]), and we carried out a counterclockwise rotation of all maps of the image A by $\theta_{\gamma_B} - \theta_{\gamma_A} = 13.63^\circ$.

We show now the final magnifications maps corresponding to the same mass distribution ($f_{\text{sdm}} = 0.1$, $F_{\text{pbh}} = 0.1$, $r_{\text{pbh}} = -2.5$) for both images, and considering $r_s = 0.605$ as for the relative source radius is concerned:

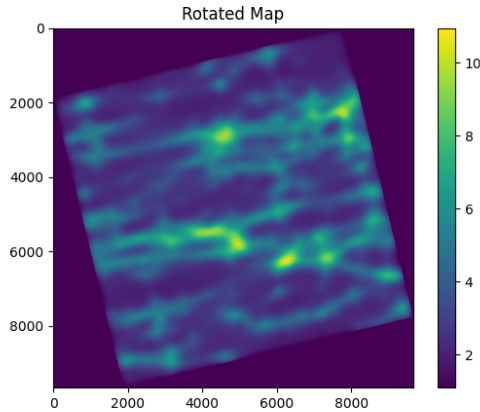


Figure 3.6: Magnification map rotated for image A in the first approach for $r_s = 0.605$

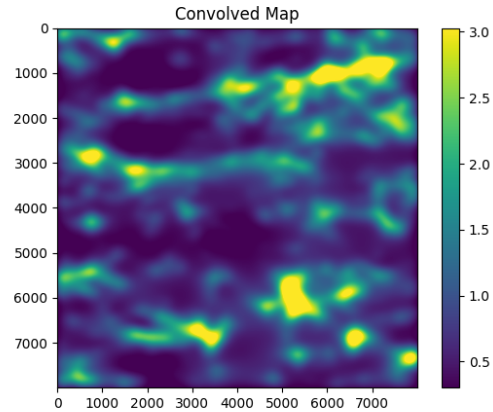


Figure 3.7: Magnification map for image B in the first approach for $r_s = 0.605$

3.3 Construction of SDLCs

Once we have generated a rotated and convolved magnification map for image A, and a convolved map for image B with the same mass configuration (i.e., the pair of AB maps were obtained from the same set of values of f_{sdm} , F_{pbh} and r_{pbh}), it is possible to draw trajectories in both maps to obtain the synthetic difference light curves, for which we have considered the source following a straight paths in the magnification maps. We have generated 10^5 SDLCs in order to have enough statistics.

Before explaining the procedure of the SDLCs construction, it is convenient to introduce the concept of the effective transverse velocity (V_e). It provides crucial information in the time domain, since it links the length of a path travelled by the source (in the source plane) to the elapsed time in the observer's rest frame. The value of V_e was estimated by [38], who obtained $V_e = 8.94 \times 10^7 \text{ cm s}^{-1}$. This effective velocity is mainly due (90% of the total) to the motion of the lens galaxy and their stars.

As far as for the trajectory construction is concerned, we have estimated the points (x_k, y_k) corresponding to N observation epochs. In particular, the point (x_0, y_0) corresponds to the first observation epoch MJD_0 and is assigned a time $t_0 = 0$. Therefore, it is possible to determine the distance travelled by the source in pixels $R_k = 0.041 \times t_k$ for the time $t_k = MJD_k - MJD_0$ in days. Taking this into account, it is possible generate a SDLC in the pair of AB maps by determining the trajectory points (x_k, y_k) :

$$\begin{aligned} x_k &= x_0 + R_k \cos \alpha \\ y_k &= y_0 + R_k \sin \alpha \end{aligned} \tag{3.3}$$

where α is chosen randomly in $[0, 2\pi]$ and represents the trajectory slope. It should be noted that although α remains the same for the pair of AB maps, the initial point (x_0, y_0) is random in both maps, i.e, the two light curves in a pair of AB maps generating a given SLDC, arise from two trajectories (one for each image map) with the same slope but different initial points.

We show in Figure 3.8 two trajectories in both maps. As one might expect from what we explained before, the same source has random initial points in both maps but equal slope.

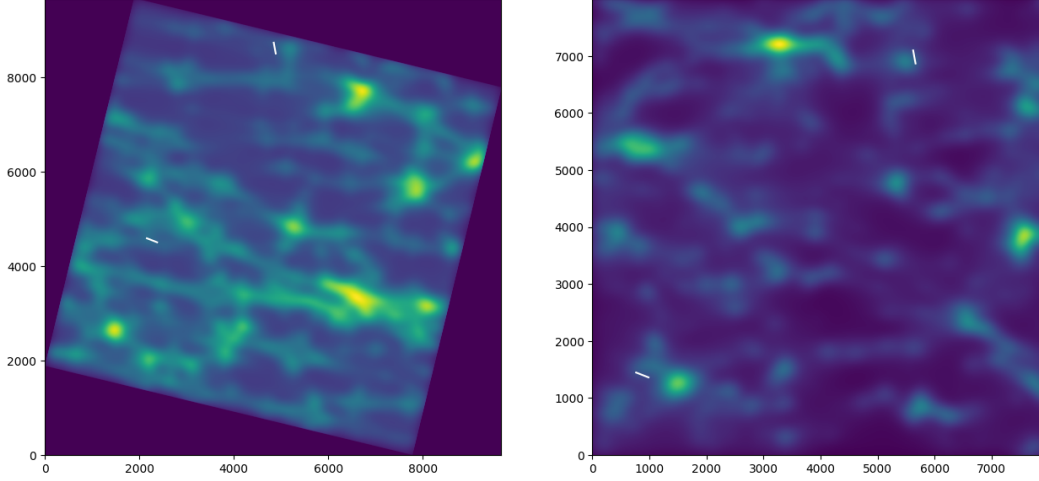


Figure 3.8: Two trajectories drawn in both magnification maps

It should be noted that both vector components of the trajectories in images A and B are real numbers and as the information in maps is saved in pixels (natural numbers), we have carried out a weighted interpolation in order to assign a magnification value at each source position (x_k, y_k) , as we can see in Figure 3.9, hence the magnification for the point (x_k, y_k) is obtained as follows:

$$\mu = \frac{w_1\mu_1 + w_2\mu_2 + w_3\mu_3 + w_4\mu_4}{w_1 + w_2 + w_3 + w_4} \quad (3.4)$$

where μ_i and w_i are the magnification and weight of the pixel i . The weights w_i are obtained depending on the distance to the four surrounding pixels centers.

Once we have assigned magnification values (μ_A or μ_B) to each point of both trajectories on the AB maps, we can use Equation (3.2), to obtain the whole SLDC for a given mass configuration and source size, either using approach 1 or 2. We now show in Figure 3.10 one of the 10^5 SLDCs obtained for the same case analysed in previous figures ($f_{\text{sdm}} = 0.1$, $F_{\text{pbh}} = 0.1$, $r_{\text{pbh}} = -2.5$ for both images, and considering $r_s = 0.605$):

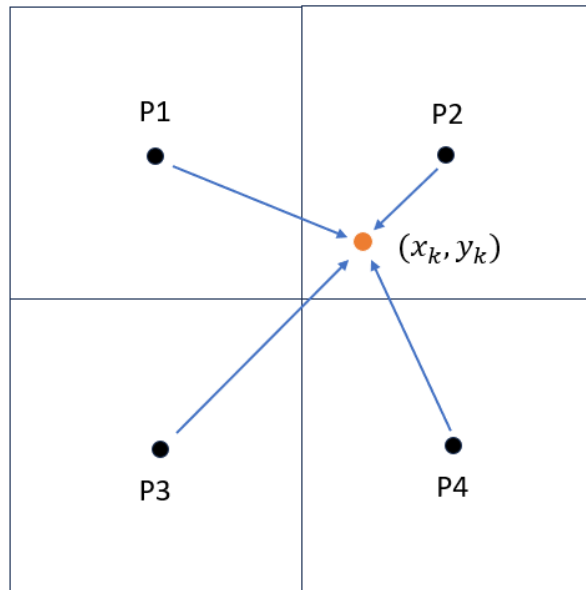


Figure 3.9: Scheme of the weighed interpolation carried out at each source position (x_k, y_k) . Figure made by the author.

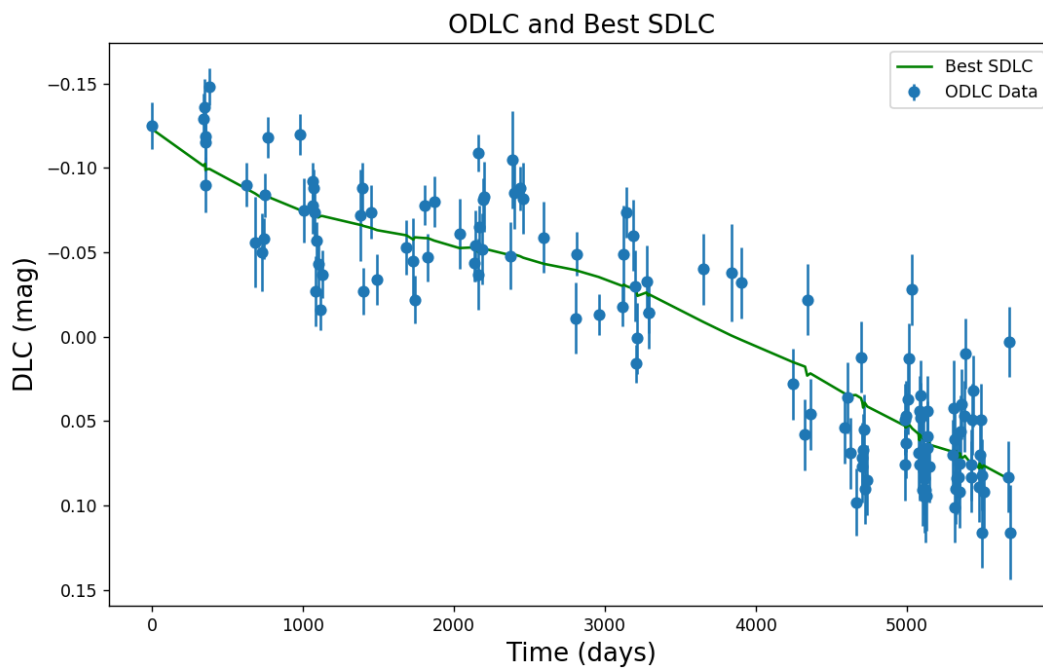


Figure 3.10: Best SDLC obtained for the scenario given by $r_s = 0.605$ and considering $f_{\text{sdm}} = 0.1$, $F_{\text{pbh}} = 0.1$, $r_{\text{pbh}} = -2.5$ in the first approach.

Furthermore it should be noted that the value of 10^5 is high enough to cover totally both magnification maps, as we can see in Figure 3.11.

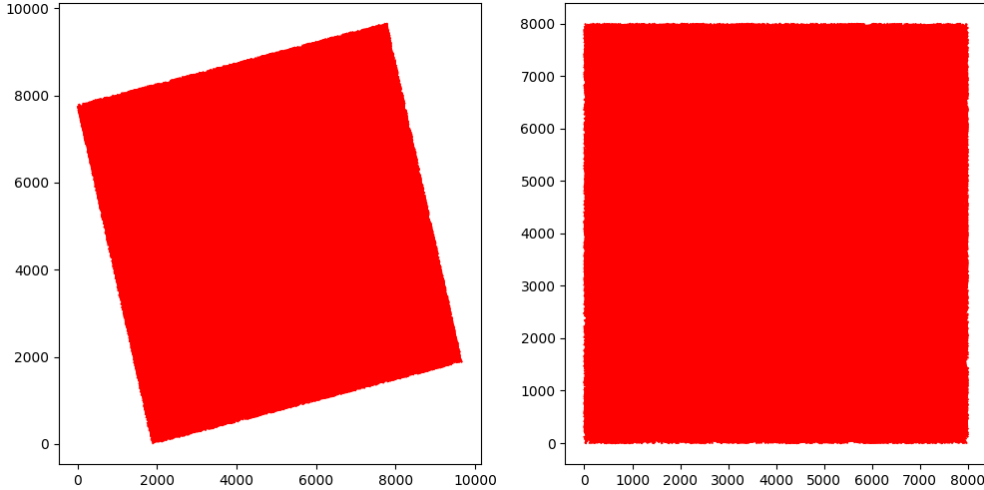


Figure 3.11: 10^5 trajectories drawn in both magnification maps: the convolved and rotated map of image A (on the left) and the convolved map of image B (on the right).

3.4 Comparison between ODLC and SDLCs

After creating 10^5 SDLCs for a given mass configuration and source size (in the first or second approach), we have to compare them with the corresponding ODLC. The method followed in this case is an statistical approach based on the Root Mean Square of Relative Residuals (RMS). This method allows us to evaluate how well the synthetic data matches the observed. Considering that the observed difference light curve consists of N data points, denoted as O_j , with their corresponding errors E_j for each point, we can denote the corresponding values for the synthetic data as M_j . Thus, the RMS for a given SDLC is determined as

$$\text{RMS} = \sqrt{\frac{1}{N} \sum_{j=1}^N \left(\frac{O_j - M_j}{E_j} \right)^2} \quad (3.5)$$

A value of Equation (3.5) close to 1 indicates a good fit between the observed and synthetic data. This suggests that the synthetic light curve is consistent with the observed data within the given uncertainties. On the contrary, a value significantly greater than 1 indicates that the synthetic light curve does not fit the observed data well, i.e, the higher the RMS, the poorer the fit. Moreover, note that a value substantially less than 1 indicates that the errors E_j are significantly overestimated, because the synthetic model fits the observed data much better than expected within the given uncertainties.

Therefore, as we have 10^5 different SDLCs, hence 10^5 RMS values, it is convenient to study the probability distribution for a given scenario (mass configuration and source size in one of the two approaches). This has been done by determining the mean and standard deviation as well as constructing the corresponding histogram in order to show how often each RMS value occurs. The ODLC-SDLC consistency threshold is set to 1.5. Thus, if the RMS distribution includes values in the range (0.5, 1.5), the SDLC is considered consistent with the observed data.

In contrast, if the RMS distribution does not include values close to 1, the scenario can be considered inconsistent with the observed data.

Although a value of 1 for RMS is ideal as it indicates a perfect fit between the synthetic model and the observed data within the given uncertainties, it is often not very realistic in practice. This is because observed data often come with slightly biased (underestimated or overestimated) errors that makes this perfect agreement difficult, hence expecting an RMS of exactly 1 is overly stringent.

Thus, we have considered an interval (0.5, 1.5) to account for a slight underestimation/overestimation of errors, the presence of a few outliers and so on. For example, $\text{RMS} = 1.5$ means measured uncertainties only represent 2/3 of real errors, which is a plausible case. However, RMS equal to 2 implies that true errors are, on average, twice as large as the measured ones, and this is inconsistent with additional tests/studies of the GLENDAMA+ data of FBQ 0951+2635. Thus, while an ODLC-SDLC consistency threshold of 2 is too permissive (accepting models that don't fit well), a threshold of 1.5 strikes a more reasonable balance by accommodating some level of discrepancy without being too lenient.

Additionally, an important decision in the analysis was the choice of the number n of SDLCs simulated per mass configuration. We have selected a value depending on the stability of the RMS distribution parameters. For instance, for a given mass configuration, we got the following results for the mean μ for six experiments with $n = 20000$ simulations each: {18.8993, 18.9861, 18.9774, 18.9653, 19.0431, 18.9977}. When increasing the value of n to $n = 100000$, we obtained {18.8861, 18.8774, 18.8653, 18.873618, 18.869118, 18.8993}. This was quite satisfactory as the maximum discrepancy was 0.17%. Moreover, when we increased the number of simulations to $n = 500000$, discrepancies were not reduced significantly and, as computational cost and time were in this case considerably high, we decided to work with $n = 100000$ SDLCs per configuration.

Chapter 4

Simulations and Results

To achieve our goal, two different approaches were used for generating magnification maps (see Section 2.6). For each approach, a total of 81 maps were created, comprising 9 mass distributions, 3 PBH masses, and 3 source sizes. The source sizes include the two values obtained [38] ($r_s = 0.605$ and 0.276) along with a third value ($r_s = 0.1$) added for comparison purposes, as it is expected to produce larger short time-scale fluctuations. Additionally, for each of these two approaches, two different schemes were used in the analysis of the corresponding simulations, as we will discuss later.

4.1 First approach

The lens mass model we have considered consists of a main lens galaxy described by an ellipsoid with a singular power-law density distribution (SPLE) and external shear from secondary lenses (ES). We have firstly generated the ODLC with the most accurate delay up to date, although it is based on old data (16 days), and compared it with SDLCs for a solution of the lens model that is based on the 16-day delay, astrophotometric constrains from HST imaging and image fluxes from radio observations, as well as spectroscopic redshifts of the system and a standard flat Λ CDM cosmology.

In a first scheme, we have assumed that simulations can reproduce the entire signal of the ODLC. Therefore, we have used the Root Mean Square (RMS) estimator to perform the analysis and comparison between the ODLC and the SDLC, whose consistency upper limit is set to 1.5.

We carried out 10^5 simulations for each scenario, and we have not found any scenario yielding SDLCs with $\text{RMS} < 1.5$. Therefore, the consistency probability (CP; ratio between the number of SDLCs leading to $\text{RMS} < 1.5$ and total number of SDLCs studied) is zero for the 81 scenarios considered in the analysis, which actually cover a wide range of mass configurations and source sizes. Thus, the results seem to be very poor, since about ten million (81×10^5) SDLCs failed to reproduce the overall behaviour of the Observed Difference Light Curve (ODLC).

As an example, we show some results obtained for a source radius $r_s = 0.605$ and a mass configuration given by $f_{\text{sdm}} = 0.9$, $F_{\text{pbh}} = 0.5$, $r_{\text{pbh}} = -0.5$: the best SDLC for that scenario ($\text{RMS} = 1.65$; Figure 4.1) and the corresponding distribution of RMS (Figures 4.2, 4.3).

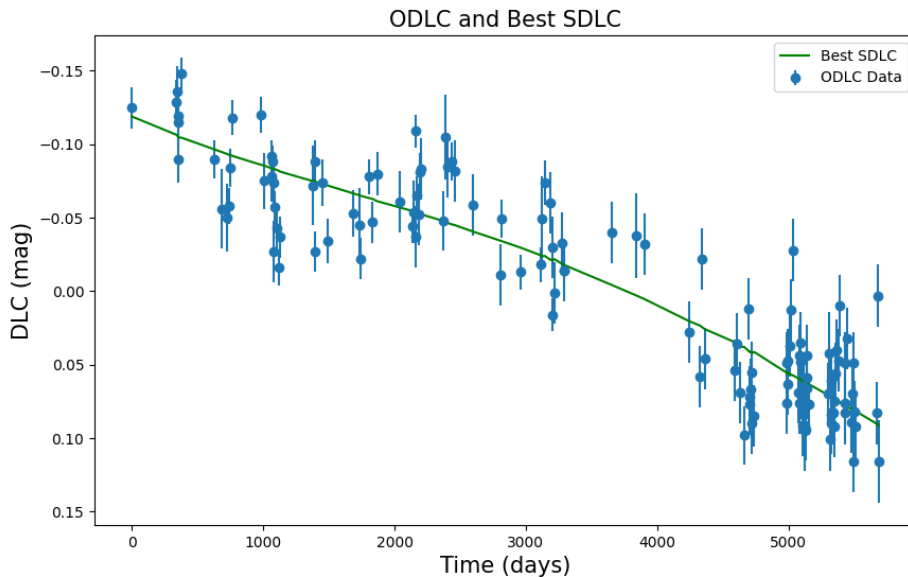


Figure 4.1: Best SDLC for the scenario studied together with the ODLc data

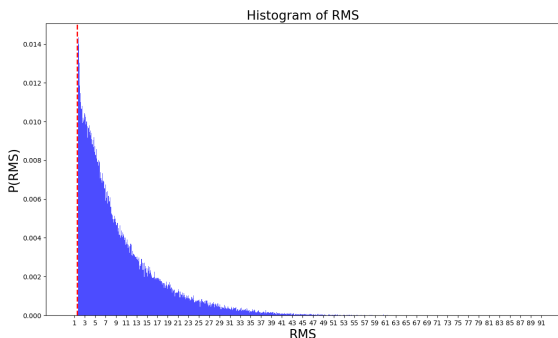


Figure 4.2: Magnification map for image A in the first approach

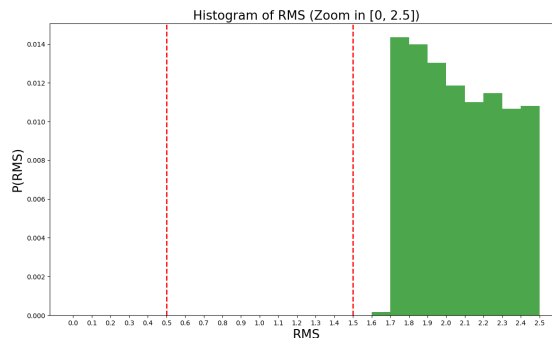


Figure 4.3: Magnification map for image B in the first approach

As far as for the other scheme is concerned, it is based on recent evidence which suggests that rapid variability in ODLcs of lensed quasars may be correlated with intrinsic rapid variability [41], so standard microlensing simulations cannot account for this kind of rapid variations in ODLcs because they ignore the intrinsic quasar variability. As a consequence, our SDLCs could only explain the slow variability observed, i.e., linear or quasi-linear gradients.

This might explain the poor results obtained in the first scheme where the SDLCs were assumed to account for the whole behaviour of the ODLc. However, in this new scheme, we consider that simulations can only reproduce the long time-scale variability of the ODLc, and this long time-scale underlying variation in which we are interested (e.g. linear or quadratic law)

is affected by uncertainties related to the fast variability and the photometric measurements. In other words, original photometric errors must be increased by a factor RMS (linear/quadratic fit) to account for the fast variability.

Alternatively, it is more convenient in this case to consider a larger ODLC-SDLC consistency threshold using original photometric errors. We have carried out a linear and a quadratic fit, calculating the corresponding RMS for both fits. We show both fits together in Figure 4.4:

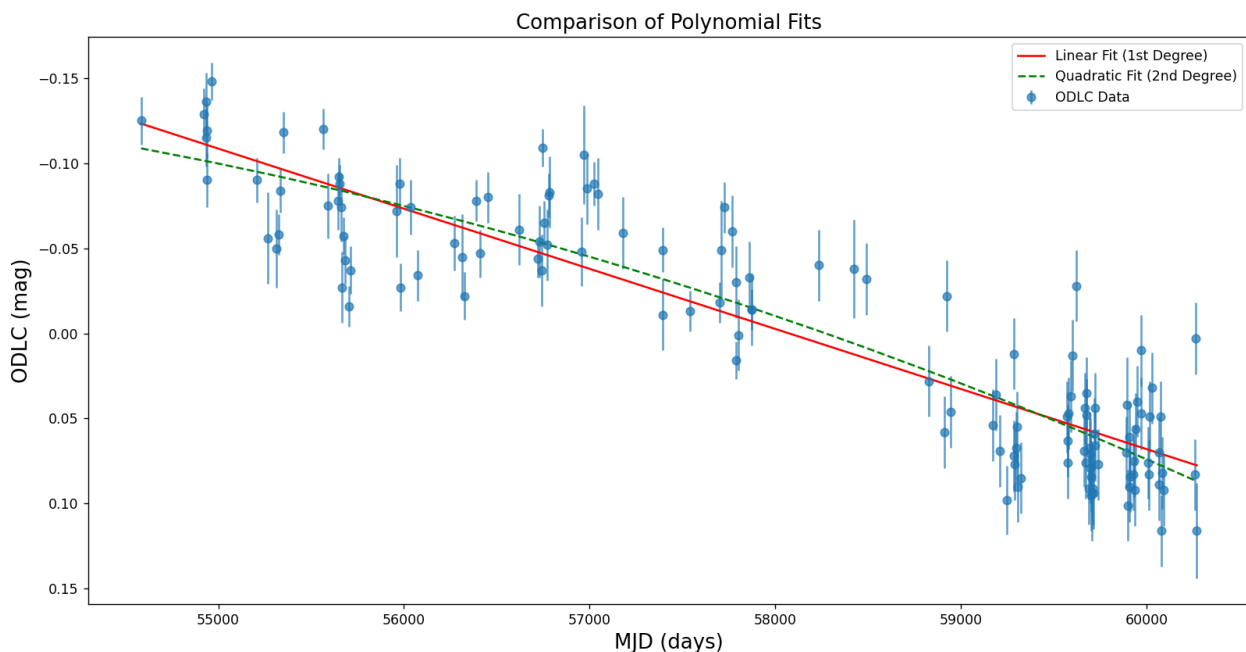


Figure 4.4: Linear and quadratic fits of the ODLC

After this, the consistency threshold for the SDLCs can be set to $1.5 \times \text{RMS}$ (linear/quadratic fit) using the original errors in the ODLC-SDLC comparisons. For the linear case, we have from Figure 4.4, $\text{RMS}(\text{linear fit}) = 1.733117$, whereas for the quadratic one, $\text{RMS}(\text{quadratic fit}) = 1.702761$, and since both fits work similarly, with a 1.8% of discrepancy in the RMS value, they have similar goodness, hence we take the linear fit as the slow underlying signal to compare with SDLCs. Thus, the results obtained for the first source size with the second scheme is shown in Table 4.1.

CP (%)	μ	σ	Conf	f_{sdm}	f_{star}	f_{pbh}	M_{pbh}
15.09	7.9449	6.8907	050925	0.5	0.05	0.45	0.001
13.34	7.6703	6.7548	090525	0.9	0.05	0.05	0.001
12.87	6.1654	5.3444	090915	0.9	0.01	0.09	10
11.60	6.0298	5.1588	090925	0.9	0.01	0.09	0.001
11.34	8.0936	7.3271	090515	0.9	0.05	0.05	10
11.32	10.1358	8.84843	090105	0.9	0.09	0.01	0.1
11.91	10.6379	9.5880	050915	0.5	0.05	0.45	10
10.99	9.9448	8.4519	090115	0.9	0.09	0.01	10
10.69	9.8315	8.0147	090505	0.9	0.05	0.05	0.1
10.57	9.9532	8.4418	090125	0.9	0.09	0.01	0.001
10.20	10.1172	8.1792	010925	0.1	0.09	0.81	0.001
8.66	13.9240	12.1765	010915	0.1	0.09	0.81	10
8.52	10.5908	8.12791	090905	0.9	0.01	0.09	0.1
6.21	13.8585	10.812	050525	0.5	0.25	0.25	0.001
6.21	14.7543	11.8658	050515	0.5	0.25	0.25	10
4.67	16.7847	13.2114	010515	0.1	0.45	0.45	10
4.20	16.9342	13.0164	050115	0.5	0.45	0.05	10
3.95	16.3179	12.1677	010525	0.1	0.45	0.45	0.001
3.74	17.2535	13.2474	050105	0.5	0.45	0.05	0.1
3.63	17.7841	13.5116	050125	0.5	0.45	0.05	0.001
2.98	18.9794	14.4261	010115	0.1	0.81	0.09	10
2.69	18.8736	13.8946	010125	0.1	0.81	0.09	0.001
2.46	17.8323	12.8318	050505	0.5	0.25	0.25	0.1
2.35	20.3822	15.1015	010105	0.1	0.81	0.09	0.1
2.04	19.7391	14.1541	010505	0.1	0.45	0.45	0.1
2.01	18.1618	12.8083	050905	0.5	0.05	0.45	0.1
1.72	20.29267	14.3280	010905	0.1	0.09	0.81	0.1

Table 4.1: Consistency probabilities for all the configurations and a source radius $r_s = 0.605$ (first approach).

As a consequence of disregarding variations on small time scales, we now find SDLCs in good agreement with the slow variation of the ODLC (the threshold now is 2.59 instead of 1.5). Moreover, the difference between configurations is notable since for instance 050925 presents a consistency probability of 15%, whereas 010905 does not reach 2%.

For instance, if we look at the less massive PBHs ($r_{\text{pbh}} = -2.5$), the average RMS is clearly correlated with f_{star} . An average RMS of approximately 6 corresponds to a mass fraction in stars of 0.01 (1%), around 8 to 5%, about 10 to 9%, roughly 14 to 25%, etc. The situation worsens as the number of stars increases, and it seems that the fraction of (less massive) PBHs doesn't play a significant role.

As an example, we show in Figure 4.5 the best SDLC obtained for the scenario 050925 (RMS = 1.63), which, as we can see, fits considerably well the slow underlying signal and the ODL data.

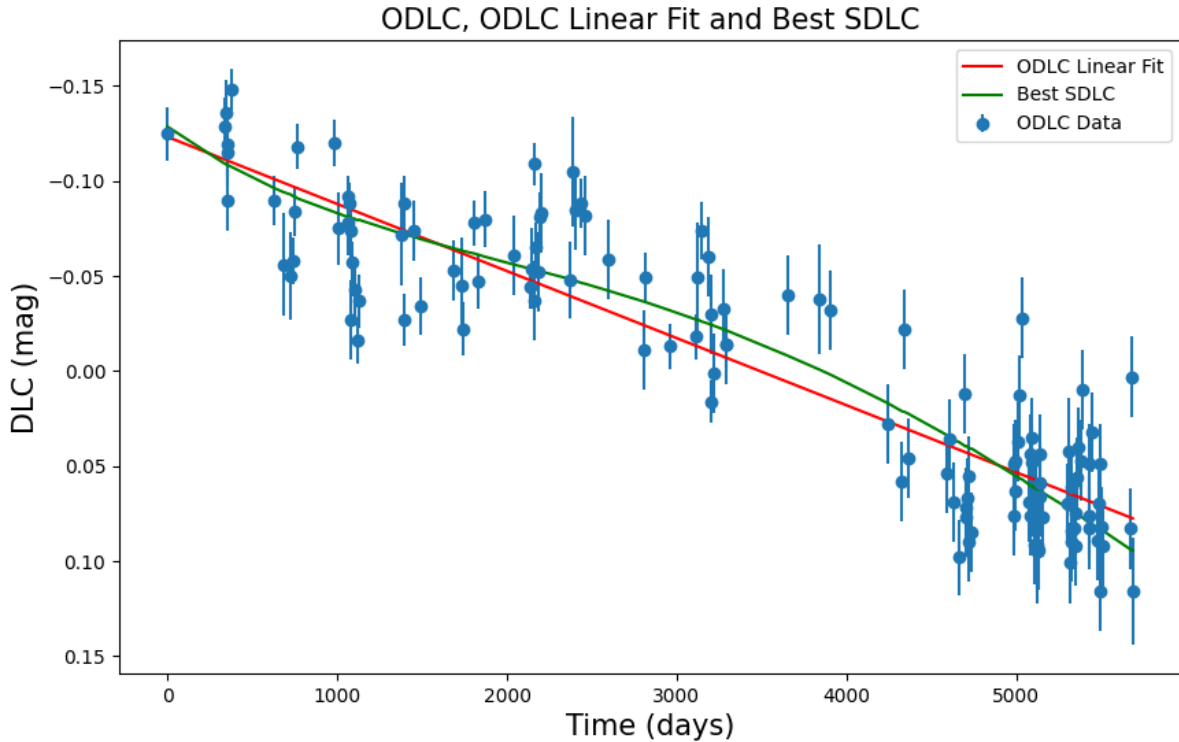


Figure 4.5: Best SDLC obtained for the best scenario 050925 ($f_{\text{sdm}} = 0.5$, $f_{\text{star}} = 0.05$ and $r_{\text{pbh}} = -2.5$) and $r_s = 0.605$, together with the ODL and the linear fit.

Furthermore, we show below the consistency probabilities for Table 4.1, in terms of M_{pbh} . They are represented in each figure by points, where its size and colour (denoted by the colour bar) indicate the value of CP for a given scenario. Therefore, in the following figures, we can appreciate visually what we mentioned before regarding the dependence of the consistency probability with the mass distribution.

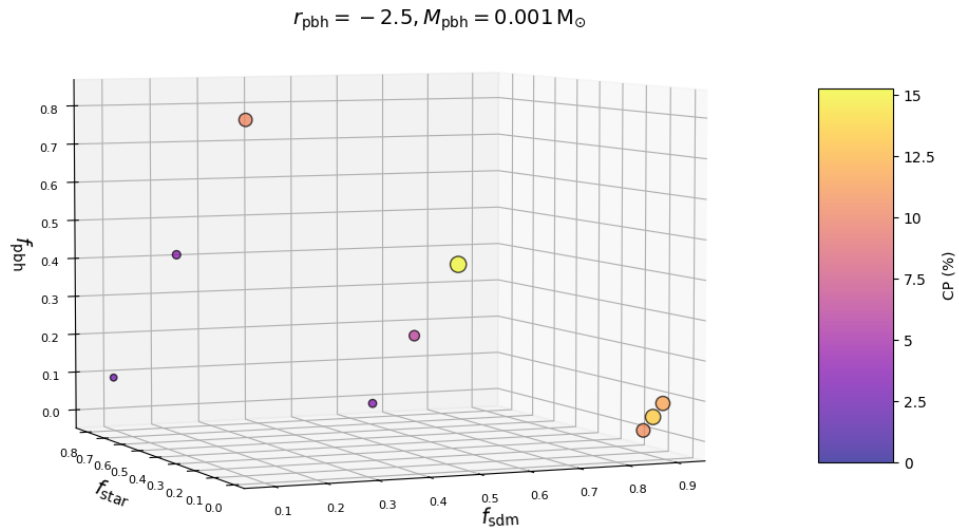


Figure 4.6: Consistency probabilities for $M_{\text{pbh}} = 0.001 M_{\odot}$ and $r_s = 0.605$ (first approach).

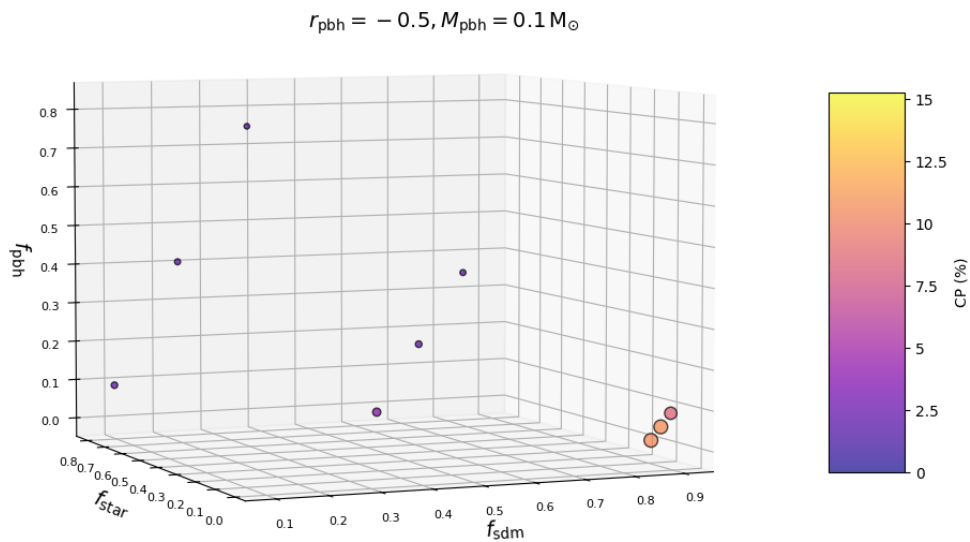


Figure 4.7: Consistency probabilities for $M_{\text{pbh}} = 0.1 M_{\odot}$ and $r_s = 0.605$ (first approach).

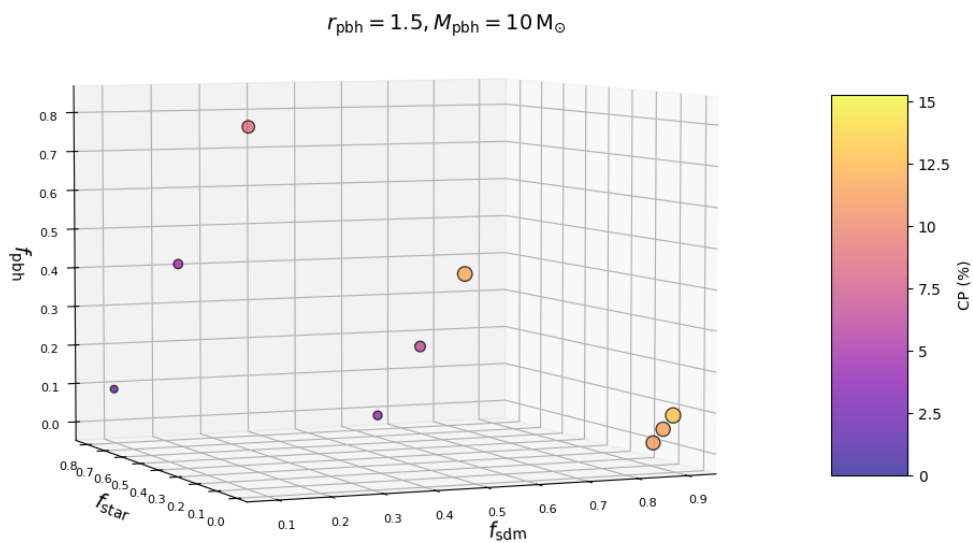


Figure 4.8: Consistency probabilities for $M_{\text{pbh}} = 10 M_{\odot}$ and $r_s = 0.605$ (first approach).

As far as for $r_s = 0.276$ is concerned, we have obtained the following results:

CP	μ	σ	Conf	f_{sdm}	f_{star}	f_{pbh}	M_{pbh}
12.28	5.8411	5.3978	090915	0.9	0.01	0.09	10
11.97	13.0029	14.3922	050915	0.5	0.05	0.45	10
10.59	9.1581	10.4328	090515	0.9	0.05	0.05	10
10.43	13.2518	13.5333	090105	0.9	0.09	0.01	0.1
9.76	13.4311	14.1017	090115	0.9	0.09	0.01	10
9.48	12.7297	13.1530	090125	0.9	0.09	0.01	0.001
8.90	14.1221	13.6695	090505	0.9	0.05	0.05	0.1
8.88	9.6128	9.7751	090525	0.9	0.05	0.05	0.001
8.24	18.4248	19.8877	010915	0.1	0.09	0.81	10
8.21	7.2666	5.7780	090925	0.9	0.01	0.09	0.001
6.22	16.4874	14.3647	090905	0.9	0.01	0.09	0.1
4.84	20.4588	18.1568	050515	0.5	0.25	0.25	10
3.53	24.2752	20.9082	010515	0.1	0.45	0.45	10
2.59	25.5019	20.9895	050115	0.5	0.45	0.05	10
2.06	26.1614	20.9364	050105	0.5	0.45	0.05	0.1
1.69	26.3315	21.1289	050125	0.5	0.45	0.05	0.001
1.47	29.3618	23.3507	010115	0.1	0.81	0.09	10
1.37	13.3708	9.8297	050925	0.5	0.05	0.45	0.001
1.34	20.8633	17.0689	050525	0.5	0.25	0.25	0.001
0.78	33.5562	25.1184	010105	0.1	0.81	0.09	0.1
0.69	31.2313	22.3376	050505	0.5	0.25	0.25	0.1
0.68	31.1520	23.1448	010125	0.1	0.81	0.09	0.001
0.67	25.4613	19.1734	010525	0.1	0.45	0.45	0.001
0.67	17.8395	12.9210	010925	0.1	0.09	0.81	0.001
0.38	34.5074	23.7598	050905	0.5	0.05	0.45	0.1
0.32	35.3162	24.4888	010505	0.1	0.45	0.45	0.1
0.17	38.8691	26.0438	010905	0.1	0.09	0.81	0.1

Table 4.2: Consistency probabilities for all configurations and a source radius $r_s = 0.276$ (first approach).

Compared to the largest source, in this case, both mean and standard deviation have generally increased significantly. Nevertheless, the SDLCs that best fit each configuration did so with RMS values lower than those for the largest source. Furthermore, we can observe that some configurations (e.g., 090915 and 050915) lead to a relatively large number of SDLCs below the consistency threshold for both source sizes. In contrast to the previous source size, we now show a bad SDLC for one of the worst scenarios (010505, see Table 4.2), that presented $\text{RMS} = 2.55$:

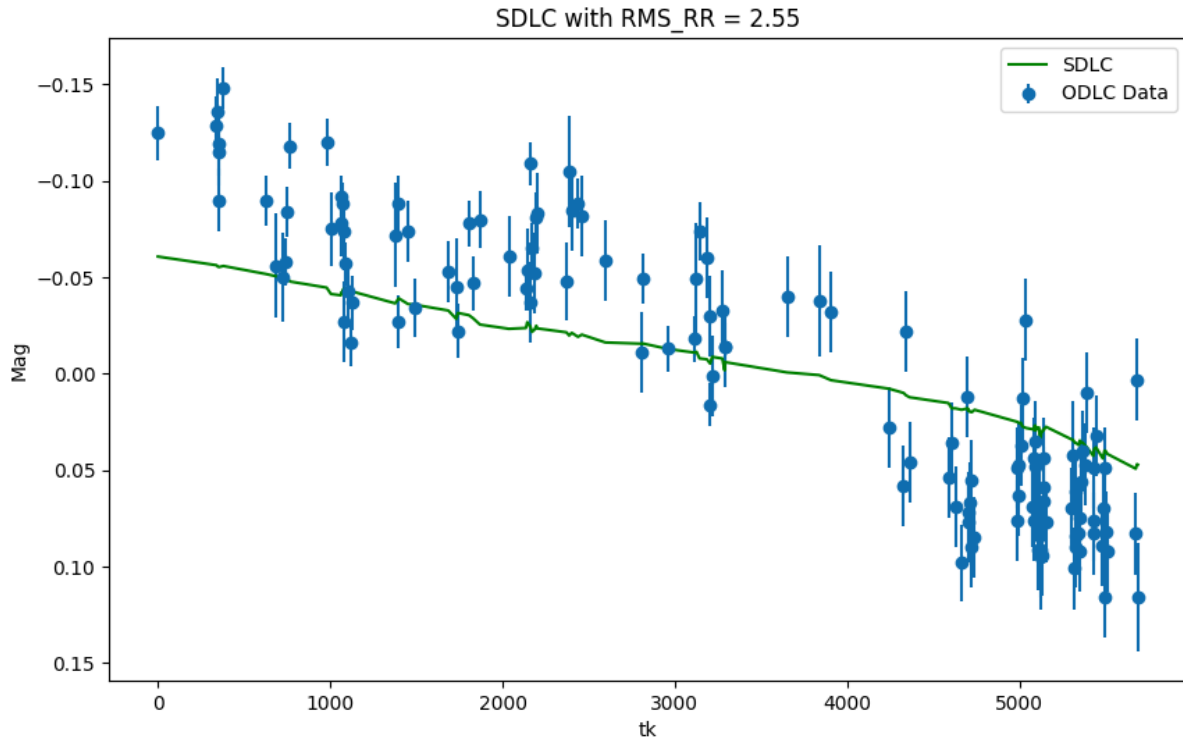


Figure 4.9: Bad SDLC for one of the worst scenarios, 010505 ($f_{\text{sdm}} = 0.1$, $f_{\text{star}} = 0.45$ and $r_{\text{pbh}} = -0.5$) and $r_s = 0.276$, together with the ODLc.

Comparing Figures 4.5 and 4.9, it is clear that the fit in the latter is significantly worse than in the former, which shows a more accurate fit to the ODLc data.

The figures corresponding to 4.2, are shown below. In this case, we can see that the points are in general much smaller than for the largest source where the colour that highlights is purple (low consistency probabilities). In addition, it can be seen that the points presenting colours close to yellow or being bigger (hence with highest CP values) correspond to scenarios with a majority contribution of SDM

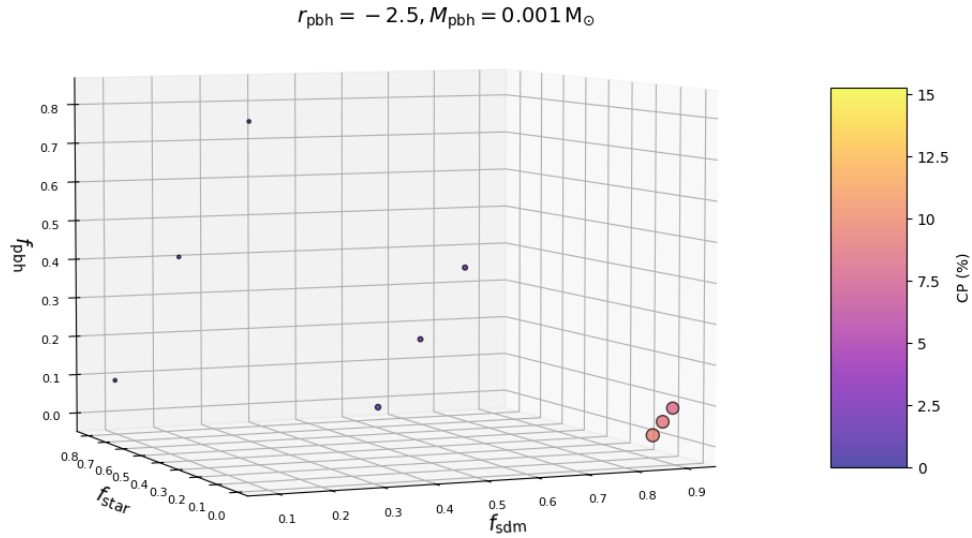


Figure 4.10: Consistency probabilities for $M_{\text{pbh}} = 0.001 M_{\odot}$ and $r_s = 0.276$ (first approach).

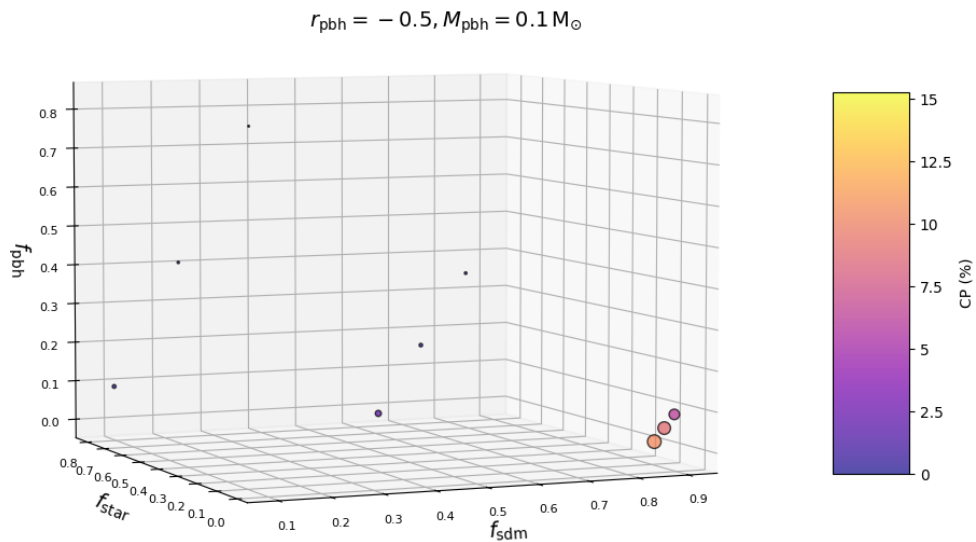


Figure 4.11: Consistency probabilities for $M_{\text{pbh}} = 0.1 M_{\odot}$ and $r_s = 0.276$ (first approach).

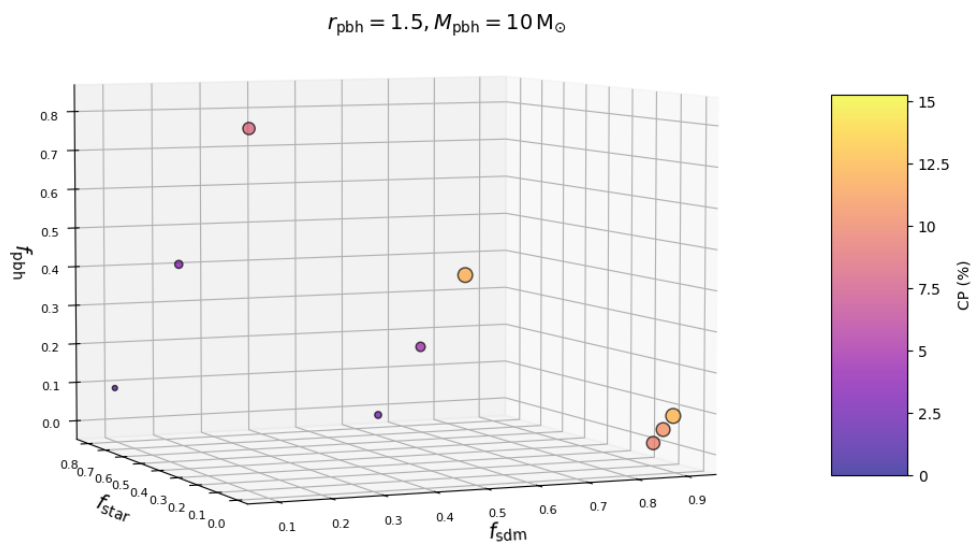


Figure 4.12: Consistency probabilities for $M_{\text{pbh}} = 10 M_{\odot}$ and $r_s = 0.276$ (first approach).

CP (%)	μ	σ	Conf	f_{sdm}	f_{star}	f_{pbh}	M_{pbh}
12.94	15.7014	20.8100	050915	0.5	0.05	0.45	10
12.41	5.6860	6.2489	090915	0.9	0.01	0.09	10
11.13	15.6052	19.2349	090105	0.9	0.09	0.01	0.1
10.88	9.6864	13.5005	090515	0.9	0.05	0.05	10
10.44	16.0237	20.3494	090115	0.9	0.09	0.01	10
9.15	16.9575	19.3625	090505	0.9	0.05	0.05	0.1
8.99	22.7024	28.5909	010915	0.1	0.09	0.81	10
6.35	20.7338	20.9888	090905	0.9	0.01	0.09	0.1
5.21	25.4941	25.2011	050515	0.5	0.25	0.25	10
3.72	16.0259	18.0289	090125	0.9	0.09	0.01	0.001
3.59	32.0099	29.7191	010515	0.1	0.45	0.45	10
2.85	33.2533	29.4409	050115	0.5	0.45	0.05	10
2.07	34.6423	29.1510	050105	0.5	0.45	0.05	0.1
1.50	39.5888	32.6845	010115	0.1	0.81	0.09	10
0.70	46.1501	34.5815	010105	0.1	0.81	0.09	0.1
0.56	43.2696	30.9945	050505	0.5	0.25	0.25	0.1
0.29	48.0860	32.8210	050905	0.5	0.05	0.45	0.1
0.20	51.7634	33.9135	010505	0.1	0.45	0.45	0.1
0.18	35.8186	28.1831	050125	0.5	0.45	0.05	0.001
0.11	16.6780	12.8954	090525	0.9	0.05	0.05	0.001
0.06	57.4081	35.7475	010905	0.1	0.09	0.81	0.1
0.03	44.9754	32.0714	010125	0.1	0.81	0.09	0.001
0.01	17.1944	8.1345	090925	0.9	0.01	0.09	0.001
0	42.3300	24.7907	010525	0.1	0.45	0.45	0.001
0	35.4664	22.2581	050525	0.5	0.25	0.25	0.001
0	42.4706	19.5058	010925	0.1	0.09	0.81	0.001
0	34.1842	14.9270	050925	0.5	0.05	0.45	0.001

Table 4.3: Consistency probabilities for all the configurations and a source radius $r_s = 0.1$ (first approach).

We observe once again, as we did with the previous cases, that in order to achieve a significant CP value, an important contribution of SDM is required (around 90%), except for the case where there is a 45% and 81% contribution from PBH, for which we have obtained notable consistency probabilities. Nevertheless, note that no case with a significant contribution from stars presents a relevant consistency probability. Additionally, it is worth noting that as we decrease the source size, the CP values tend to decrease as well (note that those with the highest values, are the ones which roughly remain the same) and that $M_{\text{pbh}} = 10M_{\odot}$ shows the highest probabilities of consistency.

In the corresponding figures of Table 4.3 (Figures 4.13, 4.14, 4.15), we can see that for this source size the consistency probabilities have decreased considerably (as most of the points are not even visible in Figures 4.13 and 4.14). In addition, as we anticipated previously, it is only in Figure 4.15 ($M_{\text{pbh}} = 10M_{\odot}$) when we have significant values for the consistency probabilities.

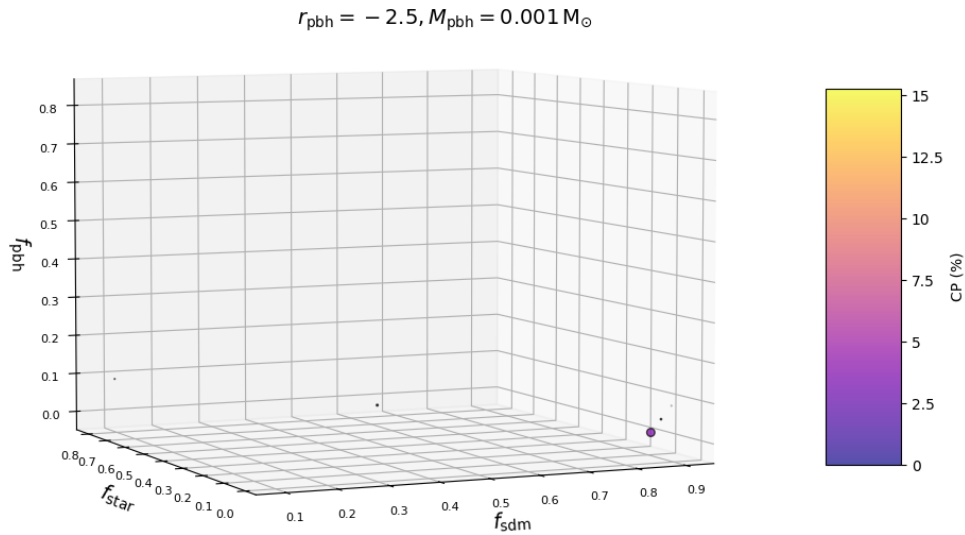


Figure 4.13: Consistency probabilities for $M_{\text{pbh}} = 0.001 M_{\odot}$ and $r_s = 0.1$ (first approach).

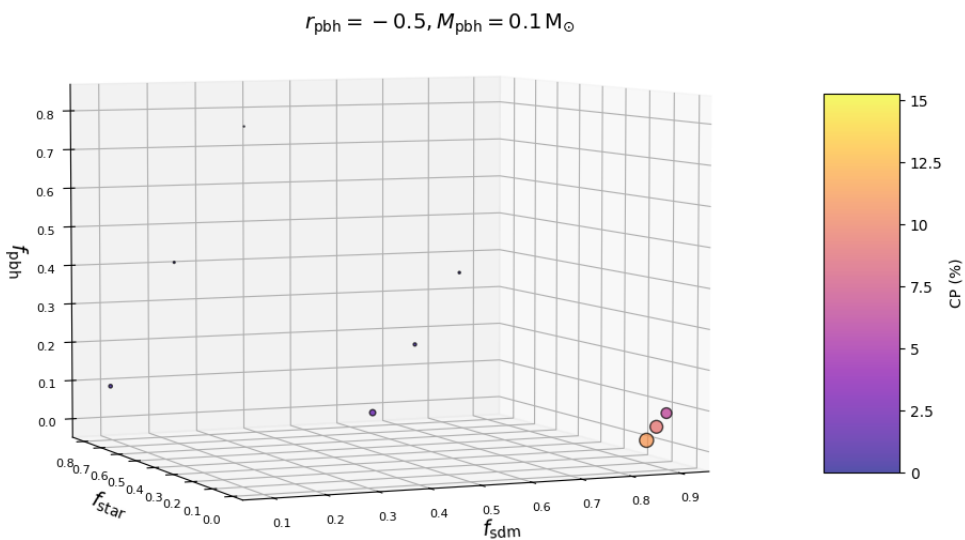


Figure 4.14: Consistency probabilities for $M_{\text{pbh}} = 0.1 M_{\odot}$ and $r_s = 0.1$ (first approach).

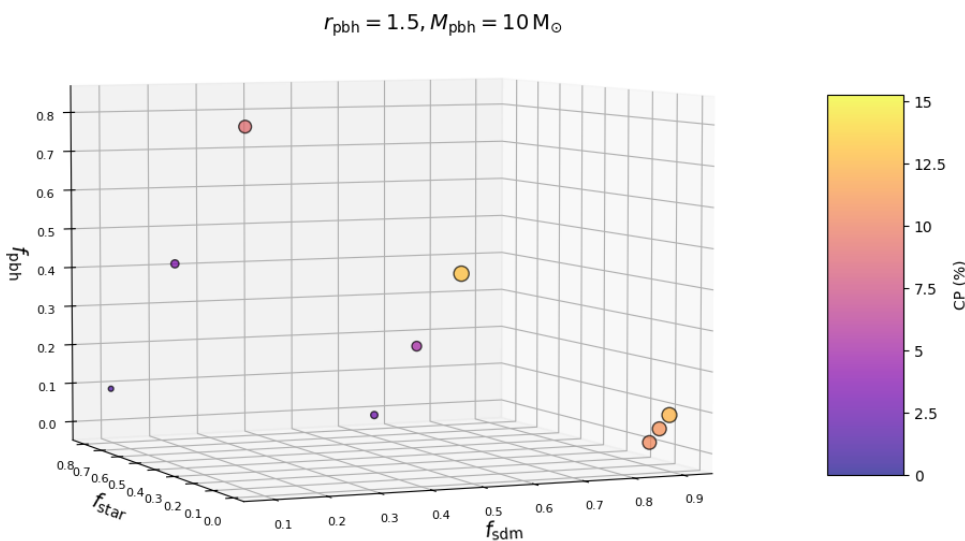


Figure 4.15: Consistency probabilities for $M_{\text{pbh}} = 10 M_{\odot}$ and $r_s = 0.1$ (first approach).

4.2 Second approach

In this second approach, we have generated the ODLC using the delay that is most consistent with all available data to date (13.3 days), in order to compare it with the SDLCs for the solution of a lensing model based on a 13.3-day delay and other observational constraints, where the SDM fraction incorporates both the contribution from the lensing galaxy itself (κ_{sdmgal}), and the additional contribution from matter halos situated close to the galaxy and along the line of sight, which act as secondary deflectors (κ_{ext}), see Section 3.2. Considering now the initial scheme as we did in the first approach, we got that the consistency probability is zero for every configuration and even for a threshold of 1.7 only a few of them are non-zero, hence reinforcing the idea that the SDLCs cannot fully reproduce the ODLC. Since the results obtained in first scheme are redundant when compared to those obtained in the first approach, we do not revisit the analysis.

Therefore, we have considered the linear fit as the slow underlying signal to compare with the SDLCs, hence in this case the threshold has been increased from 1.5 to 2.74. We show below the results obtained regarding the second scheme for the first source size.

From Table 4.4, 050925 ($f_{\text{sdmgal}} = 0.5$, $F_{\text{pbh}} = 0.9$, and $r_{\text{pbh}} = -2.5$) presents the highest consistency probability (CP= 15.25%), as took place in the first approach for this source size. In contrast, the worst scenario is 010905 (CP= 2%) corresponding to little contribution of SDM (10%) and dominant contribution of PBHs (81%).

Furthermore, if we focus again on the less massive PBHs ($r_{\text{pbh}} = -2.5$), the average RMS is once more correlated with f_{star} . An average RMS of approximately 6 corresponds to a mass fraction in stars of 0.01 (1%), around 8 to 5%, about 10 to 9%, roughly 14 to 25% and reaching 18 for 45%. Comparing the results of the two approaches for this source size, we can see that there is one scenario extra in this second approach (090505) that presents a significant value for the consistency probability (CP (%) > 10), i.e, except from this scenario, we have a clear correspondence between both approaches as far as for high values for CP is concerned.

CP (%)	μ	σ	Conf	f_{sdmgal}	f_{stargal}	f_{pbhgal}	M_{pbh}
15.25	8.2207	6.8802	050925	0.5	0.05	0.45	0.001
13.64	8.5075	7.4690	090525	0.9	0.05	0.05	0.001
13.36	10.6389	9.5674	050915	0.5	0.05	0.45	10
13.36	8.3123	8.1469	090915	0.9	0.01	0.09	10
13.33	9.3921	8.3226	090515	0.9	0.05	0.05	10
12.72	9.0745	7.8130	090115	0.9	0.09	0.01	10
12.62	6.0559	5.1064	090925	0.9	0.01	0.09	0.001
12.05	9.8690	8.2981	090125	0.9	0.09	0.01	0.001
11.78	9.6791	7.9398	010925	0.1	0.09	0.81	0.001
10.64	10.7311	8.8432	090105	0.9	0.09	0.01	0.1
9.44	13.4570	11.6357	010915	0.1	0.09	0.81	10
9.26	10.7358	8.3134	090505	0.9	0.05	0.05	0.1
8.52	10.8685	8.2227	090905	0.9	0.01	0.09	0.1
7.16	14.8164	12.1182	050515	0.5	0.25	0.25	10
7.09	13.8389	11.0235	050525	0.5	0.25	0.25	0.001
4.65	17.3328	13.6062	010515	0.1	0.45	0.45	10
3.97	17.5767	13.3403	050115	0.5	0.45	0.05	10
3.53	17.7718	13.1442	010525	0.1	0.45	0.45	0.001
3.30	17.7905	13.1085	050105	0.5	0.45	0.05	0.1
3.27	18.0630	13.3025	050125	0.5	0.45	0.05	0.001
2.87	17.8611	12.7613	050505	0.5	0.25	0.25	0.1
2.55	20.9620	15.6200	010115	0.1	0.81	0.09	10
2.52	20.3683	15.1645	010125	0.1	0.81	0.09	0.001
2.39	17.9556	12.5685	050905	0.5	0.05	0.45	0.1
2.36	20.2514	14.6692	010105	0.1	0.81	0.09	0.1
2.20	20.4076	14.8376	010505	0.1	0.45	0.45	0.1
2.00	20.6557	14.7333	010905	0.1	0.09	0.81	0.1

Table 4.4: Consistency probabilities for all the combinations analysed in the second approach for the size $r_s = 0.605$.

Additionally, comparing the following figures with those from the first approach (Figures 4.6, 4.7 and 4.8), we can see they are quite similar.

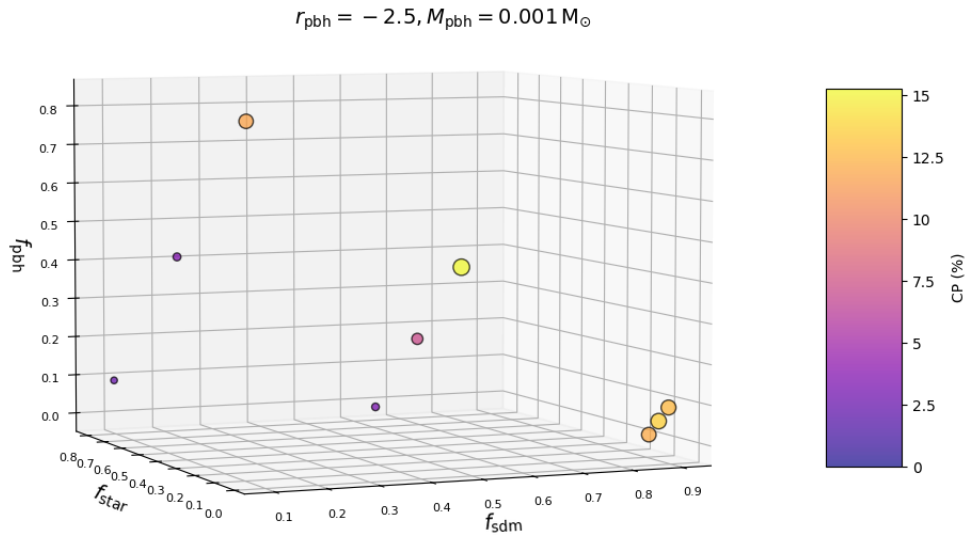


Figure 4.16: Consistency probabilities for $M_{\text{pbh}} = 0.001 M_{\odot}$ and $r_s = 0.605$ (second approach).

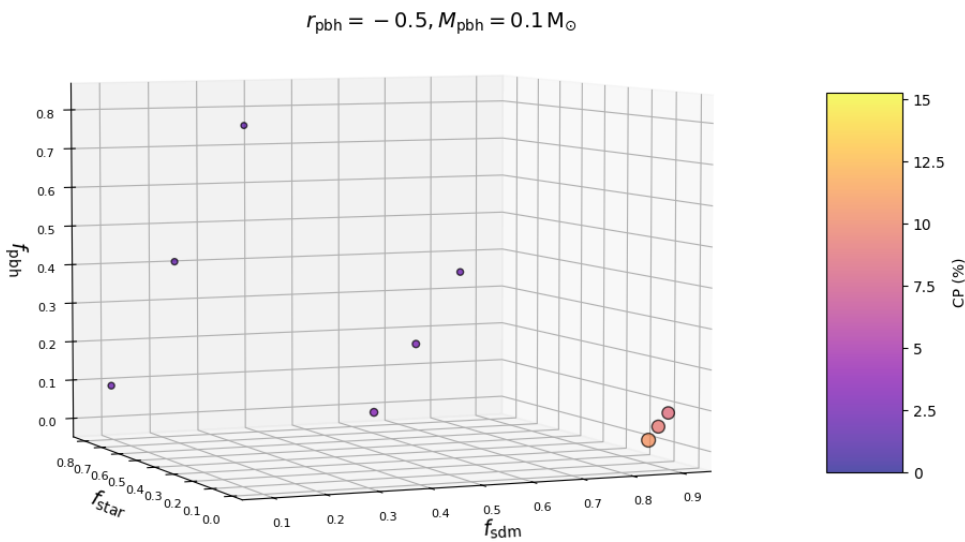


Figure 4.17: Consistency probabilities for $M_{\text{pbh}} = 0.1 M_{\odot}$ and $r_s = 0.605$ (second approach).

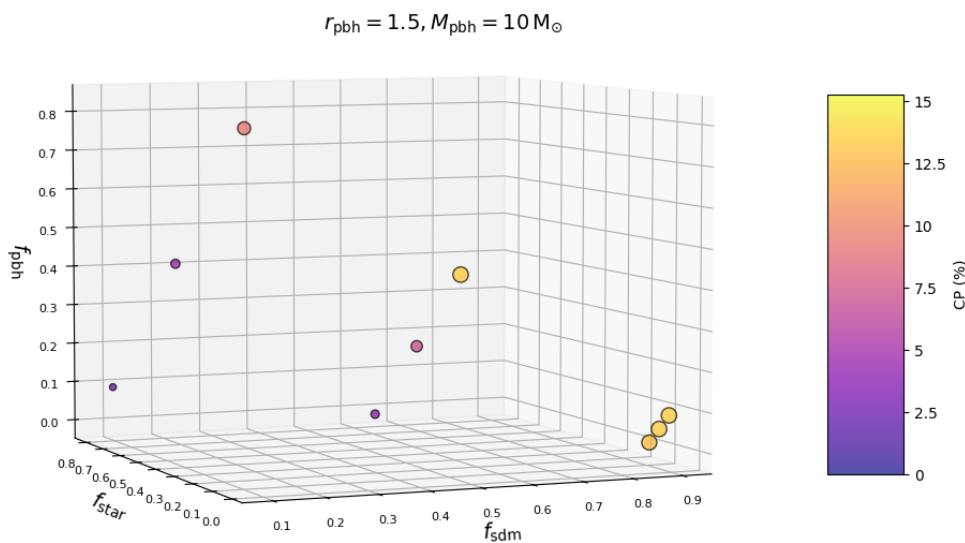


Figure 4.18: Consistency probabilities for $M_{\text{pbh}} = 10 M_{\odot}$ and $r_s = 0.605$ (second approach).

Considering now the second source size:

CP (%)	μ	σ	Conf	f_{sdmgal}	f_{stargal}	f_{pbhgal}	M_{pbh}
13.42	12.7500	14.2782	050915	0.5	0.05	0.45	10
13.34	9.0553	12.0530	090915	0.9	0.01	0.09	10
12.88	11.4433	13.0124	090515	0.9	0.05	0.05	10
11.17	12.0744	12.5202	090115	0.9	0.09	0.01	10
10.72	12.9071	13.3651	090125	0.9	0.09	0.01	0.001
9.68	7.3544	5.9056	090925	0.9	0.01	0.09	0.001
9.52	11.2378	11.7065	090525	0.9	0.05	0.05	0.001
9.17	17.7124	18.6583	010915	0.1	0.09	0.81	10
9.15	14.8579	14.4778	090105	0.9	0.09	0.01	0.1
7.07	16.5960	14.8761	090505	0.9	0.05	0.05	0.1
6.22	20.1196	18.9120	050515	0.5	0.25	0.25	10
5.39	18.0061	15.0634	090905	0.9	0.01	0.09	0.1
3.19	26.1924	22.4627	010515	0.1	0.45	0.45	10
2.14	26.8277	21.2932	050115	0.5	0.45	0.05	10
1.70	27.9915	21.7661	050105	0.5	0.45	0.05	0.1
1.64	20.8974	17.4120	050525	0.5	0.25	0.25	0.001
1.56	13.8653	10.2419	050925	0.5	0.05	0.45	0.001
1.46	27.7928	21.5766	050125	0.5	0.45	0.05	0.001
0.95	32.6786	25.0285	010115	0.1	0.81	0.09	10
0.78	17.4083	12.6283	010925	0.1	0.09	0.81	0.001
0.75	33.3374	24.8743	010125	0.1	0.81	0.09	0.001
0.66	28.0134	20.9408	010525	0.1	0.45	0.45	0.001
0.64	32.7695	23.8587	010105	0.1	0.81	0.09	0.1
0.61	32.5485	22.9828	050505	0.5	0.25	0.25	0.1
0.26	37.8529	26.1102	010505	0.1	0.45	0.45	0.1
0.26	36.0418	24.1950	050905	0.5	0.05	0.45	0.1
0.14	40.4576	26.7451	010905	0.1	0.09	0.81	0.1

Table 4.5: Consistency probabilities for all the combinations analysed in the second approach for the size $r_s = 0.276$.

As one might infer from Table 4.5, the results are once more correlated with those in the first approach since only one scenario in the second approach with $\text{CP} > 10$ does not in the first one (090105), although these values are slightly higher in this second approach. Moreover, in this case, the influence of the PBH masses is noticeable, as the four best scenarios present $M_{\text{pbh}} = 10M_{\odot}$, whereas the five worst present $M_{\text{pbh}} = 0.1M_{\odot}$. This is reproduced in the following figures:

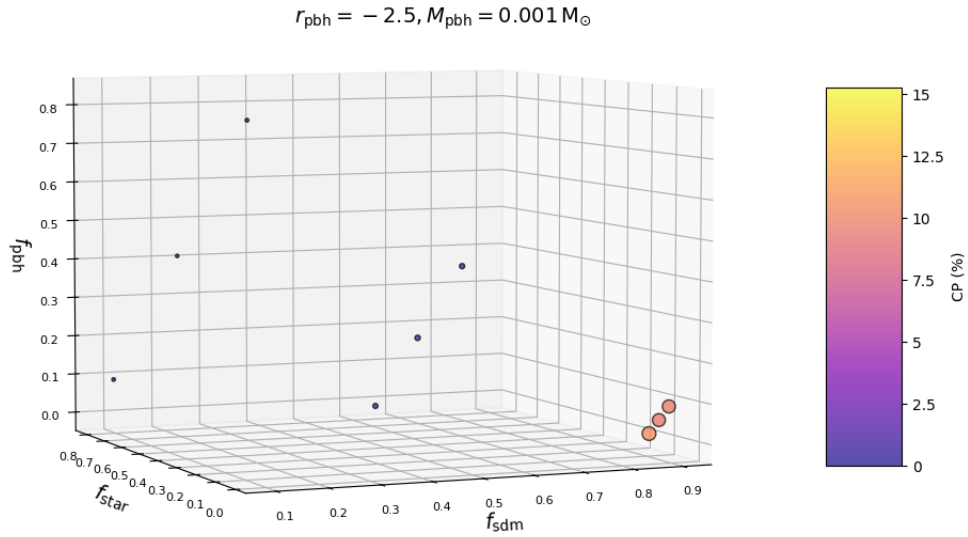


Figure 4.19: Consistency probabilities for $M_{\text{pbh}} = 0.001 M_{\odot}$ and $r_s = 0.276$ (second approach).

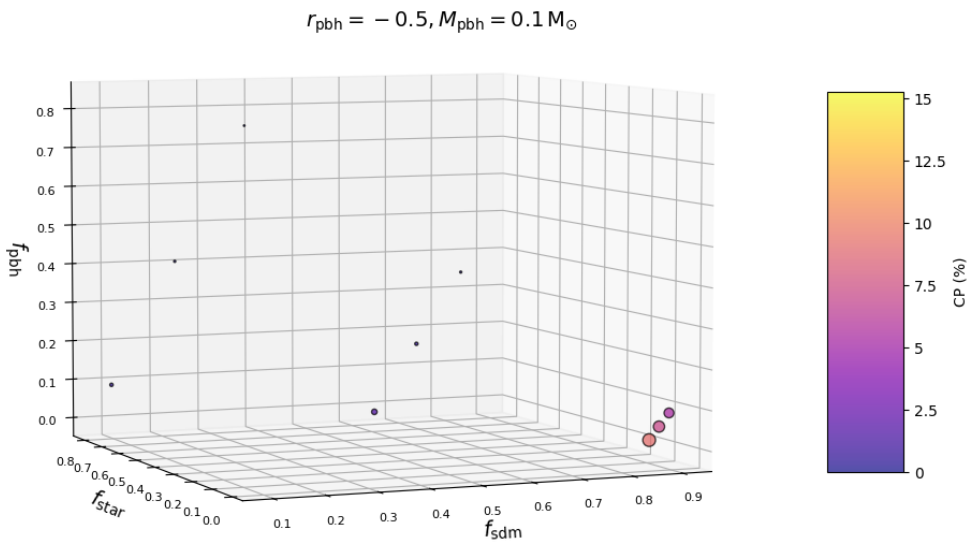


Figure 4.20: Consistency probabilities for $M_{\text{pbh}} = 0.1 M_{\odot}$ and $r_s = 0.276$ (second approach).

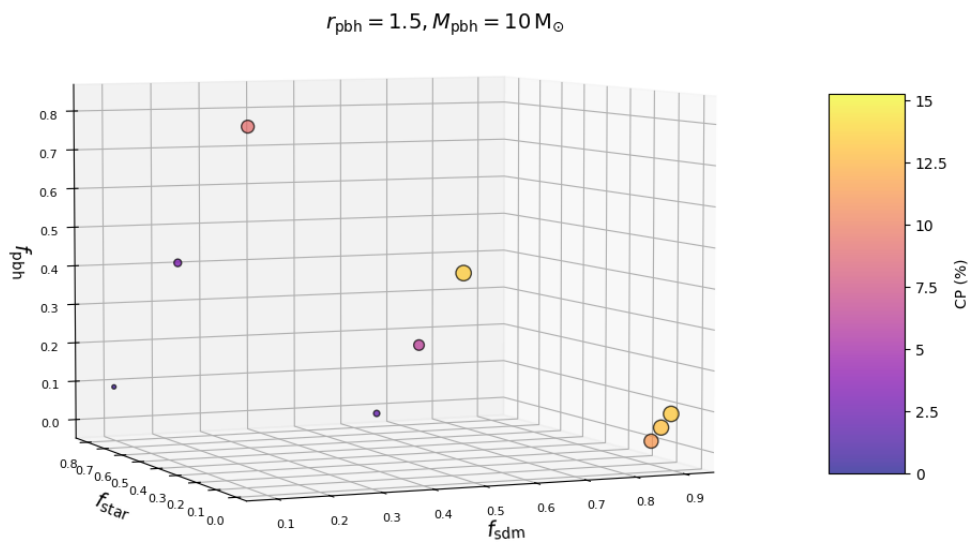


Figure 4.21: Consistency probabilities for $M_{\text{pbh}} = 10 M_{\odot}$ and $r_s = 0.276$ (second approach).

We show eventually the results for the smallest source in Table 4.6, which are quite similar as those in the first approach, following the general trend.

CP (%)	μ	σ	Conf	f_{sdmgal}	f_{stargal}	f_{pbhgal}	M_{pbh}
14.63	14.6099	19.8237	050915	0.5	0.05	0.45	10
14.04	9.6801	16.3822	090915	0.9	0.01	0.09	10
13.88	12.7988	17.9370	090515	0.9	0.05	0.05	10
11.84	14.3969	18.2492	090115	0.9	0.09	0.01	10
9.86	21.7985	26.2997	010915	0.1	0.09	0.81	10
9.51	17.8804	20.5609	090105	0.9	0.09	0.01	0.1
7.19	20.3742	21.1797	090505	0.9	0.05	0.05	0.1
6.77	24.7930	26.2713	050515	0.5	0.25	0.25	10
5.33	23.1277	22.1791	090905	0.9	0.01	0.09	0.1
3.92	16.3073	18.3693	090125	0.9	0.09	0.01	0.001
3.26	34.6482	31.9371	010515	0.1	0.45	0.45	10
2.17	35.4320	29.3481	050115	0.5	0.45	0.05	10
1.56	36.2141	29.8413	050105	0.5	0.45	0.05	0.1
1.03	44.7637	34.7826	010115	0.1	0.81	0.09	10
0.60	46.5437	33.1998	010105	0.1	0.81	0.09	0.1
0.55	45.3393	32.0065	050505	0.5	0.25	0.25	0.1
0.19	52.1561	33.7830	050905	0.5	0.05	0.45	0.1
0.15	55.6943	35.8544	010505	0.1	0.45	0.45	0.1
0.11	37.4724	28.8557	050125	0.5	0.45	0.05	0.001
0.06	18.3219	15.6957	090525	0.9	0.05	0.05	0.001
0.04	47.8108	34.4214	010125	0.1	0.81	0.09	0.001
0.04	60.4993	36.4507	010905	0.1	0.09	0.81	0.1
0	17.1775	8.2810	090925	0.9	0.01	0.09	0.001
0	44.5187	26.9417	010525	0.1	0.45	0.45	0.001
0	35.3541	22.6108	050525	0.5	0.25	0.25	0.001
0	41.4340	18.5459	010925	0.1	0.09	0.81	0.001
0	34.2592	15.2915	050925	0.5	0.05	0.45	0.001

Table 4.6: Consistency probabilities for all the combinations analysed in the second approach for the size $r_s = 0.1$.

Analogously as in the first approach, both mean and standard deviation are the highest among the three source sizes considered. Furthermore, $M_{\text{pbh}} = 10M_{\odot}$ is required in this case to present a significant consistency probability since every scenario with $\text{CP} > 10$ exhibit this value for the PBHs mass.

The corresponding figures are shown below, where the point that highlights in Figure 4.24 presents an important contribution of SDM (50%) and PBHs (45%) in the lensing galaxy (which is the scenario 050915 we have already mentioned before).

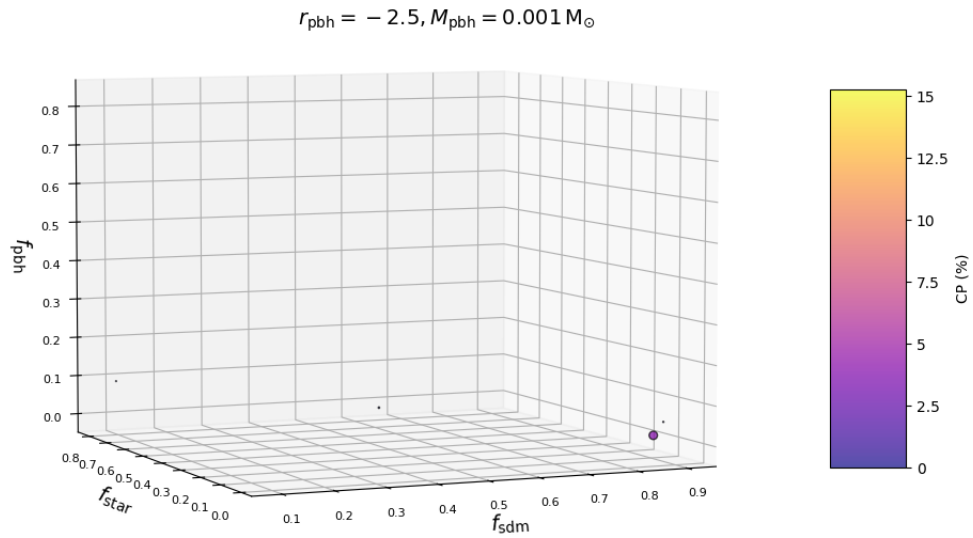


Figure 4.22: Consistency probabilities for $M_{\text{pbh}} = 0.001 M_{\odot}$ and $r_s = 0.1$ (second approach).

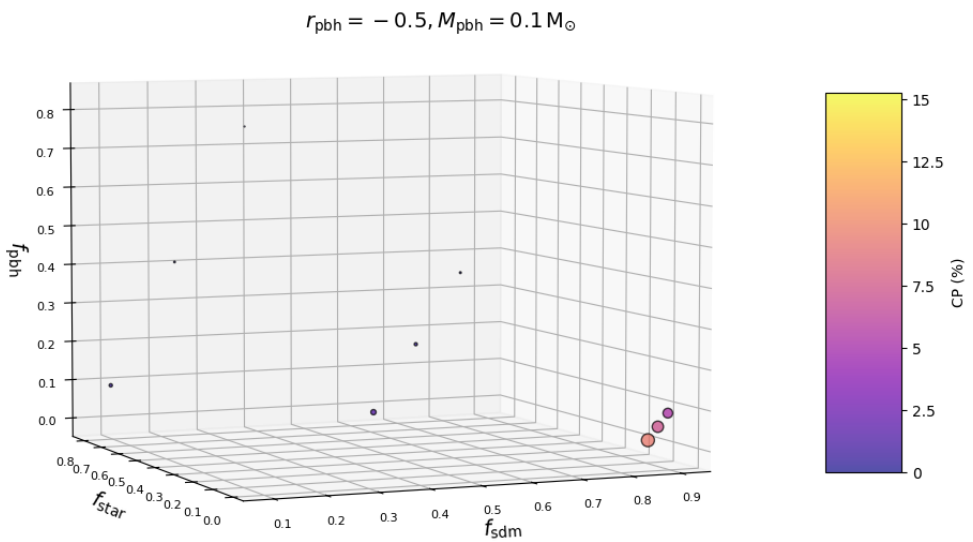


Figure 4.23: Consistency probabilities for $M_{\text{pbh}} = 0.1 M_{\odot}$ and $r_s = 0.1$ (second approach).

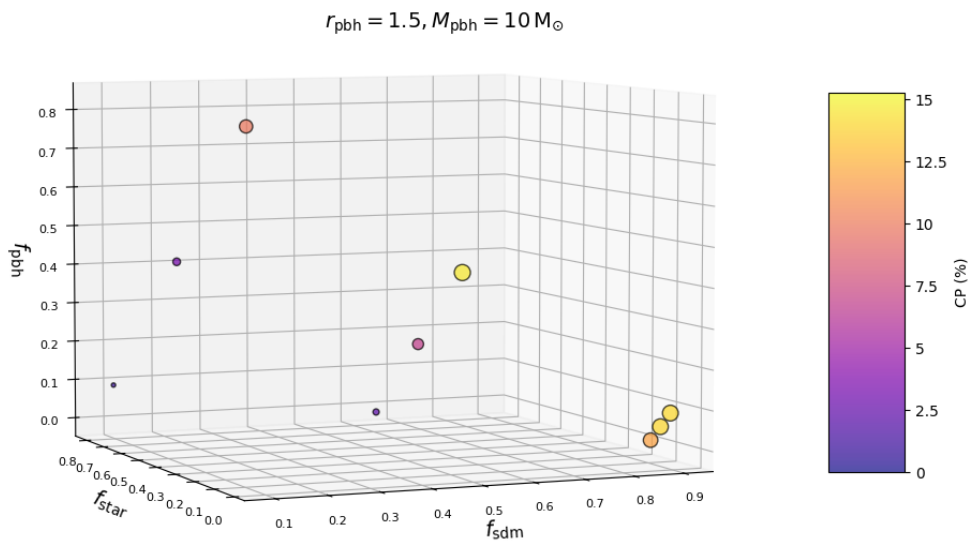


Figure 4.24: Consistency probabilities for $M_{\text{pbh}} = 10 M_{\odot}$ and $r_s = 0.1$ (second approach).

Chapter 5

Conclusions

Through our study, we have shown that gravitational lensing is a crucial tool in astrophysics, offering a unique way to explore and understand the universe. In particular, using two different approaches, we have tried to give light and obtain constraints on possible PBH populations in the non-local early-type galaxy acting as a gravitational lens of the doubly imaged gravitationally lensed quasar FBQ 0951+2635.

We have obtained quite similar results in both approaches, so considering a refined time delay between quasar images and an observationally-based external convergence does not significantly alter the results from an early delay and the hypothesis $\kappa_{\text{ext}} = 0$.

The most critical role is played by the scheme we used to analyse our microlensing simulations, i.e., the criterion to compare synthetic (simulated) difference light curves with the observed one. Despite analyzing 81 scenarios covering a wide range of mass distributions in the lens galaxy, PBH masses, and source sizes, none of them are consistent with the observed extrinsic variability on all time scales. Hence, if simulations are forced to reproduce all observed variations, we can reject all tested PBH populations. The situation is very different if simulations should only reproduce the underlying long time-scale variation. This second scheme is consistent with recent results for another double quasar [41] and preliminary tests for FBQ 0951+2635, and leads to encouraging conclusions.

In both approaches, it is clear that the condition for an ODLC-SDLC consistency probability above 10% is a small contribution from stars ($f_{\text{star}} < 10\%$) and a significant/dominant contribution from smoothly distributed matter ($f_{\text{sdm}} = 50/90\%$). The only exception is a scenario with $f_{\text{sdm}} = 10\%$, $f_{\text{star}} = 9\%$, $f_{\text{pbh}} = 81\%$, and $M_{\text{pbh}} = 0.001$ solar masses for the largest source. Notably, the scenario with $f_{\text{sdm}} = 50\%$, $f_{\text{star}} = 5\%$, $f_{\text{pbh}} = 45\%$, and $M_{\text{pbh}} = 10$ solar masses exhibits a relatively high CP for all three source sizes. Also noteworthy is the relatively high consistency probability for $f_{\text{sdm}} = 50\%$, $f_{\text{star}} = 5\%$, $f_{\text{pbh}} = 45\%$, $M_{\text{pbh}} = 0.001$ solar masses, and the largest source. Furthermore, in general terms, the consistency probability decrease when the source size is decreased.

Using our second comparison scheme, the main conclusion is that several scenarios including a significant (and even dominant) population of primordial black holes of 0.001 or 10 solar masses cannot be completely ruled out because they have a probability exceeding 10%.

Esteban-Gutiérrez et al. [23] also compared optical fluxes for nine quadruply imaged quasars (single-epoch fluxes, not light curves) and microlensing simulations for typical values of the quasar redshift ($z_{\text{qso}} = 2$), lens redshift ($z_{\text{gal}} = 0.5$), and convergence and shear ($\kappa = \gamma = 0.45$). They considered a standard population of stars in the lens galaxy, and ruled out a dominant population of PBHs with $M_{\text{pbh}} = 30$ solar masses (a typical mass for black holes detected through GW experiments). Additionally, [42] analysed light curves of six lensed quasars spanning ~ 10 years. They explored if observed microlensing signals were consistent with reasonable populations of stars or whether additional microlenses (e.g., PBHs) are required. They concluded that a standard scenario without non-stellar microlenses cannot be rejected, in contrast with a previous study by Hawkins [43], who claimed that a population of PBHs with stellar mass is required to account for the microlensing signal in light curves of lensed quasars.

Given the results obtained in this work, it is crucial to go further and carry out more detailed studies. One idea could be improving of the resolution of the parameter grid ($f_{\text{star}}, F_{\text{pbh}}, M_{\text{pbh}}, r_s$), as a finer resolution in these parameters will allow for a more accurate exploration of their respective influences and interdependencies, potentially leading to new insights into their roles in galaxies. It could be also interesting to consider a distribution of M_{pbh} covering a wider range of values which could help us in improving our understanding of how different PBH mass might affect the results. Another important direction for future research might be analyzing light curves with a significantly greater temporal coverage, e.g. $\sim 25 - 30$ years, hence a more robust dataset, as well as expanding the study to include a larger number of lensing systems (quasars undergoing lensing and microlensing effects), which could result in obtaining new and strong constraints.

Bibliography

- [1] Planck Collaboration et al. “Planck2018 results: VI. Cosmological parameters”. In: *Astronomy and Astrophysics* 641 (Sept. 2020), A6. DOI: [10.1051/0004-6361/201833910](https://doi.org/10.1051/0004-6361/201833910).
- [2] NASA Science. *Building Blocks of the Universe*. Accessed: 2024-08-14. 2024. URL: <https://science.nasa.gov/universe/overview/building-blocks/>.
- [3] A. Secchi. *L’Astronomia in Roma nel pontificato di Pio IX: memoria*. Tipografia della Pace, 1877.
- [4] W. T. Kelvin. *Baltimore Lectures on Molecular Dynamics and the Wave Theory of Light*. <https://doi.org/10.1017/CB09780511694523>. Cambridge University Press, 2010.
- [5] F. Zwicky. “Nebulae as Gravitational Lenses”. In: *Phys. Rev.* 51.4 (1937), pp. 290–290. DOI: [10.1103/PhysRev.51.290](https://doi.org/10.1103/PhysRev.51.290).
- [6] V. C. Rubin et al. “Extended rotation curves of high-luminosity spiral galaxies. IV. Systematic dynamical properties”. In: *The Astrophysical Journal* 225 (1978), pp. 107–111. DOI: [10.1086/182804](https://doi.org/10.1086/182804).
- [7] V. C. Rubin et al. “Rotational properties of 21 SC galaxies with a large range of luminosities and radii”. In: *The Astrophysical Journal* 238 (1980), pp. 471–487. DOI: [10.1086/158003](https://doi.org/10.1086/158003).
- [8] Y. B. Zel’dovich and I. D. Novikov. “The Hypothesis of Cores Retarded during Expansion and the Hot Cosmological Model”. In: *Sov. Astron.* 10 (1967), p. 602.
- [9] B. J. Carr and S. W. Hawking. “Black holes in the early Universe”. In: 168 (Aug. 1974), pp. 399–416. DOI: [10.1093/mnras/168.2.399](https://doi.org/10.1093/mnras/168.2.399).
- [10] S. W. Hawking. “Particle creation by black holes”. In: *Communications in Mathematical Physics* 43.3 (1975), pp. 199–220. DOI: [10.1007/BF02345020](https://doi.org/10.1007/BF02345020).
- [11] Wikipedia contributors. *List of gravitational wave observations*. Wikipedia, The Free Encyclopedia. Last accessed: 29 August 2024. 2024. URL: https://en.wikipedia.org/wiki/List_of_gravitational_wave_observations.
- [12] B. Carr and F. Kuhnel. “Primordial Black Holes as Dark Matter: Recent Developments”. In: *Annual Review of Nuclear and Particle Science* 70 (2020), pp. 355–394. DOI: [10.1146/annurev-nucl-050520-125911](https://doi.org/10.1146/annurev-nucl-050520-125911).
- [13] J. L. Bernal et al. “Cosmological implications of primordial black holes”. In: *Journal of Cosmology and Astroparticle Physics* 2017.10 (2017), p. 052. DOI: [10.1088/1475-7516/2017/10/052](https://doi.org/10.1088/1475-7516/2017/10/052).
- [14] I. Newton. *Opticks*. Dover Press, 1704. URL: <https://doi.org/10.5479/sil.302475.39088000644674>.

- [15] M. Meneghetti. *Introduction to Gravitational Lensing: With Python Examples*. 1st ed. Lecture Notes in Physics. Springer Cham, 2021, pp. XIII, 412. DOI: [10.1007/978-3-030-73582-1](https://doi.org/10.1007/978-3-030-73582-1).
- [16] J. G. von Soldner. “Über die Ablenkung der Lichtstrahlen durch die Sonne”. In: *Memoirs of the Royal Bavarian Academy of Sciences* 1 (1804). Translated as "On the Deflection of Light Rays by the Sun", pp. 161–236.
- [17] A. Einstein. “On the Influence of Gravitation on the Propagation of Light”. In: *Annalen der Physik* 35 (1911). Page 906 is where the main result is discussed, pp. 898–908. DOI: [10.1002/andp.200590033](https://doi.org/10.1002/andp.200590033).
- [18] J. Wambsganss. “Gravitational Lensing in Astronomy”. In: *Living Reviews in Relativity* 1.1 (1998), p. 12. DOI: [10.12942/lrr-1998-12](https://doi.org/10.12942/lrr-1998-12). URL: <https://doi.org/10.12942/lrr-1998-12>.
- [19] O. Chwolson. “Über eine mögliche Form fiktiver Doppelsterne”. In: *Astronomische Nachrichten* 221 (1924). In German: "On a Possible Form of Fictitious Binary Stars", p. 329.
- [20] F. Zwicky. “On the Probability of Detecting Nebulae Which Act as Gravitational Lenses”. In: *Physical Review Letters* 51 (1937), p. 679. DOI: [10.1103/PhysRev.51.290](https://doi.org/10.1103/PhysRev.51.290).
- [21] S. Refsdal. “On the Possibility of Determining Hubble’s Parameter and the Masses of Galaxies from the Gravitational Lens Effect”. In: *Monthly Notices of the Royal Astronomical Society* 128.4 (1964), pp. 307–310. DOI: [10.1093/mnras/128.4.307](https://doi.org/10.1093/mnras/128.4.307).
- [22] R. Carswell D. Walsh and R. Weymann. “0957 + 561 A, B: Twin Quasistellar Objects or Gravitational Lens?” In: *Nature* 279 (1979), pp. 381–384. DOI: [10.1038/279381a0](https://doi.org/10.1038/279381a0).
- [23] A. Esteban-Gutiérrez et al. “Limiting the Abundance of LIGO/Virgo Black Holes with Microlensing Observations of Quasars of Finite Size”. In: *The Astrophysical Journal Letters* 929.1 (2022), p. L17. DOI: [10.3847/2041-8213/ac57c6](https://doi.org/10.3847/2041-8213/ac57c6).
- [24] G. Vernardos et al. “Microlensing of Strongly Lensed Quasars”. In: 220.1, 14 (Feb. 2024), p. 14. DOI: [10.1007/s11214-024-01043-8](https://doi.org/10.1007/s11214-024-01043-8).
- [25] R. Narayan and S. Wallington. “Introduction to basic concepts of gravitational lensing”. In: *Gravitational Lenses*. Ed. by T. Schramm R. Kayser and L. Nieser. Berlin, Heidelberg: Springer Berlin Heidelberg, 1992, pp. 12–26.
- [26] P. Dokkum et al. “A massive compact quiescent galaxy at $z = 2$ with a complete Einstein ring in JWST imaging”. In: *Nature Astronomy* 8 (Oct. 2023), pp. 1–7. DOI: [10.1038/s41550-023-02103-9](https://doi.org/10.1038/s41550-023-02103-9).
- [27] C. Keeton. “Software for Gravitational Lensing”. In: (2001).
- [28] C. R. Keeton. *Strong Lens Modeling: Principles and Basic Methods*. Talk presented at the XXIV Canary Islands Winter School of Astrophysics: Astrophysical Applications of Gravitational Lensing. Nov. 2012.

- [29] P. L. Schechter et al. “The First FIRST Gravitationally Lensed Quasar: FBQ 0951+2635*”. In: *The Astronomical Journal* 115.4 (1998), p. 1371. DOI: [10.1086/300294](https://doi.org/10.1086/300294).
- [30] P. Jakobsson et al. “An optical time delay for the double gravitational lens system FBQ 0951+2635*”. In: *A&A* 431.1 (2005), pp. 103–109. DOI: [10.1051/0004-6361:20041432](https://doi.org/10.1051/0004-6361:20041432).
- [31] F. Courbin A. Eigenbrod and G. Meylan. “COSMOGRAIL: the COSmological MONitoring of GRAVItational Lenses: VI. Redshift of the lensing galaxy in seven gravitationally lensed quasars”. In: *Astronomy & Astrophysics* 465.1 (2007), pp. 51–56. DOI: [10.1051/0004-6361:20066939](https://doi.org/10.1051/0004-6361:20066939).
- [32] E. A. Ruiz Hinojosa. “Cosmología mediante cúasares dobles”. MA thesis. Universidad de Cantabria, July 2023. URL: <https://hdl.handle.net/10902/30820>.
- [33] M. L. Wilson et al. “A Spectroscopic Survey of the Fields of 28 Strong Gravitational Lenses: Implications for H₀”. In: *The Astrophysical Journal* 850.1 (2017), p. 94. DOI: [10.3847/1538-4357/aa9653](https://doi.org/10.3847/1538-4357/aa9653).
- [34] V. N. Shalyapin, R. Gil-Merino, and L. J. Goicoechea. “Fast simulations of extragalactic microlensing”. In: 653, A121 (Sept. 2021), A121. DOI: [10.1051/0004-6361/202140527](https://doi.org/10.1051/0004-6361/202140527).
- [35] C. S. Kochanek. “Quantitative Interpretation of Quasar Microlensing Light Curves”. In: 605.1 (Apr. 2004), pp. 58–77. DOI: [10.1086/382180](https://doi.org/10.1086/382180).
- [36] M. A. Cornachione et al. “Near-infrared and Optical Continuum Emission Region Size Measurements in the Gravitationally lensed Quasars Q0957+561 and SBS0909+532”. In: 905.1, 7 (Dec. 2020), p. 7. DOI: [10.3847/1538-4357/abc25d](https://doi.org/10.3847/1538-4357/abc25d).
- [37] V. N. Shalyapin et al. “Resolving the inner accretion flow towards the central supermassive black hole in SDSS J1339+1310”. In: *A&A* 646 (2021), A165. DOI: [10.1051/0004-6361/202038770](https://doi.org/10.1051/0004-6361/202038770).
- [38] A. B. Rivera et al. “Optical and Near-infrared Continuum Emission Region Size Measurements in the Lensed Quasar FBQ J0951+2635”. In: *The Astrophysical Journal* 952.1 (2023), p. 54. DOI: [10.3847/1538-4357/acdb4f](https://doi.org/10.3847/1538-4357/acdb4f).
- [39] A. Gould. “Measuring the Remnant Mass Function of the Galactic Bulge”. In: 535.2 (June 2000), pp. 928–931. DOI: [10.1086/308865](https://doi.org/10.1086/308865).
- [40] E. Paic et al. “Constraining quasar structure using high-frequency microlensing variations and continuum reverberation”. In: *A&A* 659 (2022), A21. DOI: [10.1051/0004-6361/202141808](https://doi.org/10.1051/0004-6361/202141808).
- [41] V. N. Shalyapin L. J. Goicoechea and A. Oscoz. “Apparent correlation between extrinsic and intrinsic flux variations in the first gravitationally lensed quasar”. In: *Monthly Notices of the Royal Astronomical Society* 530.2 (2024), pp. 2273–2281. DOI: [10.1093/mnras/stae952](https://doi.org/10.1093/mnras/stae952).
- [42] P. Awad et al. “Probing compact dark matter objects with microlensing in gravitationally lensed quasars”. In: *AA* 673 (2023), A88. DOI: [10.1051/0004-6361/202245615](https://doi.org/10.1051/0004-6361/202245615).

- [43] M. R. S. Hawkins. “The signature of primordial black holes in the dark matter halos of galaxies”. In: *Astronomy amp; Astrophysics* 633 (Jan. 2020), A107. DOI: [10.1051/0004-6361/201936462](https://doi.org/10.1051/0004-6361/201936462).

Chapter A

Appendix: Python programs

A.1 Convolution and Rotation of Magnification Maps

```
1 import numpy as np
2 import matplotlib.pyplot as plt
3 from astropy.convolution import convolve_fft, Gaussian2DKernel
4 from scipy import ndimage
5
6 # Input filename from the user
7 filename = input("Enter the name of the .bin file (without extension): ")
8 input_file = filename + '.bin'
9
10 # Reading and showing the original map
11 data = np.fromfile(input_file, '<f4')
12 N = int(np.sqrt(len(data))) # determine image size NxN
13 print(N)
14
15 image = data.reshape((N, N))
16 # tune appropriate vmin, vmax
17 plt.imshow(image, vmin=image.mean()*0.25, vmax=image.mean()*4)
18 plt.title('Original Map')
19 plt.savefig(filename + '.png')
20 plt.show()
21
22 ## Convolution with a 2D Gaussian
23 # rE = 200 pix
24 # rs = 0.605: Rs = 200*rs = 121 pix          #First source size
25
26 #gauss = Gaussian2DKernel(121)
27
28 # Convolution with a 2D Gaussian
29 # rE = 200 pix
30 # rs = 0.276: Rs = 200*rs = 55.2 pix        #Second source size
31
32 # Convolution with a 2D Gaussian
33 # rE = 200 pix
34 # rs = 0.1: Rs = 200*rs = 20 pix           #Third source size
35
36 gauss = Gaussian2DKernel(121)
37
```

```
38
39 ## Carry out the convolution and save the results
40 cimage = convolve_fft(image, gauss, allow_huge=True)           #Convolution
41
42 conv_filename = filename + '_c.npy'
43 np.save(conv_filename, cimage)
44
45 plt.imshow(cimage, vmin=image.mean()*0.3, vmax=image.mean()*3)
46 # tune appropriate vmin, vmax
47 plt.colorbar()
48 plt.title('Convolved Map')
49 plt.savefig(filename + '_c.png')
50 plt.show()
51
52 ##Loading the file to check it is correct
53
54 b = np.load(conv_filename)
55 plt.imshow(b, vmin=image.mean()*0.3, vmax=image.mean()*3)
56 plt.show()
57
58 # Counterclockwise rotation of 13.63 deg and save the results
59 crimage = ndimage.rotate(cimage, 13.63, reshape=True)         #Rotation
60
61 rot_filename = filename + '_r.npy'
62 np.save(rot_filename, crimage)
63
64 plt.imshow(crimage, vmin=image.mean()*0.3, vmax=image.mean()*3)
65 plt.colorbar()
66 plt.title('Rotated Map')
67 plt.savefig(filename + '_r.png')
68 plt.show()
69
70 ##Loading the file to check it is correct
71
72 c = np.load(rot_filename)
73 plt.imshow(c, vmin=image.mean()*0.3, vmax=image.mean()*3)
74 plt.show()
```

A.2 Main Program: SDLCs construction and analysis

```
1 import os
2 import numpy as np
3 import sys
4 import math
5 import matplotlib.pyplot as plt
6 from scipy.optimize import curve_fit
7 from scipy.stats import norm
8 import time
9
10 # Record the start time
11 start_time = time.time()
12
13 filenameA = sys.argv[1]
14 filenameB = sys.argv[2]
15 crmap = np.load(filenameA)
16 crmapB = np.load(filenameB)
17
18 # Extract the relevant part of the first file name (removing "_A_r")
19 base_nameA = filenameA.split('_')[0][:-1]
20 pi = np.pi
21 rows, cols = crmap.shape
22 scale = cols
23
24 file_path = 'q0951DLC.dat' # File containing the ODLIC data
25 data = np.loadtxt(file_path)
26 col1 = data[:, 0]
27 Oj = data[:, 1]
28 Ej = data[:, 2]
29 tk = col1 - col1[0]
30 N = len(tk)
31
32 R_tk = 0.041 * tk
33
34 # Define the linear function for the linear fit
35 def linear_model(tk, m, b):
36     return m * tk + b
37
38 # Perform the linear fit
39 popt, pcov = curve_fit(linear_model, tk, Oj, sigma=Ej)
40
41 # Extract the fitted parameters
42 m, b = popt
43
44 # Generate the fitted values
45 Oj_fit = linear_model(tk, m, b)
46 RMS_RR_lin = np.sqrt(np.sum(((Oj - Oj_fit) / Ej) ** 2) / N)
47 knorm = RMS_RR_lin
```

```

48 threshold = 1.5 * knorm
49 print(f"The threshold is {threshold}.")
50
51 # Plot the original data and the linear fit
52 plt.figure(figsize=(10, 6))
53 plt.errorbar(tk, Oj, yerr=Ej, fmt='o', label='Observed Data')
54 plt.plot(tk, Oj_fit, label='Linear Fit', color='red')
55 plt.xlabel('tk')
56 plt.ylabel('Oj')
57 plt.legend()
58 plt.gca().invert_yaxis() # Invert Y-axis
59 fit_path = os.path.join(output_dir, 'linear_fit.png')
60 plt.savefig(fit_path) # Save the figure before displaying it
61 plt.show()
62 plt.close()
63
64 valid_results = []
65 Mk_components_A = [[] for _ in range(len(R_tk))]
66
67 rowsB, colsB = crmapB.shape
68 scaleB = colsB
69
70 valid_results_B = []
71 Mk_components_B = [[] for _ in range(len(R_tk))]
72
73 # Define the number of simulations
74 Nsim = 100000
75
76 RMS_RR_values = []
77 # List to store valid SDLCS data
78 valid_SDLCSdata_SDLCS = []
79 valid_SDLCSdata_SDLCS_strict = []
80 min_RMS_RR = float('inf')
81 best_SDLCS = None
82 Nsimv = 0
83
84 for sim in range(Nsim):
85     while True:
86
87         #We first create the trajectories
88         x0 = np.random.uniform(0, scale)
89         y0 = np.random.uniform(0, scale)
90         phi = np.random.uniform(0, 2 * np.pi)
91
92         xk = x0 + R_tk * np.cos(phi)
93         yk = y0 + R_tk * np.sin(phi)
94
95         x0_B = np.random.uniform(0, scaleB)
96         y0_B = np.random.uniform(0, scaleB)

```

```

97     xk_B = x0_B + R_tk * np.cos(phi)
98     yk_B = y0_B + R_tk * np.sin(phi)
99
100     if np.any(xk < 0) or np.any(xk >= scale) or \
101        np.any(yk < 0) or np.any(yk >= scale):
102         continue
103     if np.any(xk_B < 0) or np.any(xk_B >= scaleB)\
104        or np.any(yk_B < 0) or np.any(yk_B >= scaleB):
105         continue
106
107     Mk = np.zeros(len(xk))
108     Mk_B = np.zeros(len(xk_B))
109
110     #We carry out the weighed interpolation
111     for idx in range(len(xk)):
112         x_current = xk[idx]
113         y_current = yk[idx]
114         floor_x = math.floor(x_current)
115         floor_y = math.floor(y_current)
116
117         if floor_x + 1 >= rows or floor_y + 1 >= cols:
118             continue
119
120         d1k = math.sqrt((x_current - floor_x) ** 2 \
121            + (y_current - floor_y) ** 2)
122         d2k = math.sqrt((x_current - (floor_x + 1)) ** 2 \
123            + (y_current - floor_y) ** 2)
124         d3k = math.sqrt((x_current - floor_x) ** 2 + \
125            (y_current - (floor_y + 1)) ** 2)
126         d4k = math.sqrt((x_current - (floor_x + 1)) ** 2 \
127            + (y_current - (floor_y + 1)) ** 2)
128         W1 = 1 - d1k
129         W2 = 1 - d2k
130         W3 = 1 - d3k
131         W4 = 1 - d4k
132         M1 = cmap[floor_x, floor_y]
133         M2 = cmap[floor_x + 1, floor_y]
134         M3 = cmap[floor_x, floor_y + 1]
135         M4 = cmap[floor_x + 1, floor_y + 1]
136         Mk[idx] = (M1 * W1 + M2 * W2 + M3 * W3 + M4 * W4) / (W1 + W2 \
137            + W3 + W4)
138
139     for idx in range(len(xk_B)):
140         x_current = xk_B[idx]
141         y_current = yk_B[idx]
142         floor_x = math.floor(x_current)
143         floor_y = math.floor(y_current)
144
145         if floor_x + 1 >= rowsB or floor_y + 1 >= colsB:

```

```

146         continue
147
148         d1k_B = math.sqrt((x_current - floor_x) ** 2 + \
149         (y_current - floor_y) ** 2)
150         d2k_B = math.sqrt((x_current - (floor_x + 1)) ** 2 \
151         + (y_current - floor_y) ** 2)
152         d3k_B = math.sqrt((x_current - floor_x) ** 2 \
153         + (y_current - (floor_y + 1)) ** 2)
154         d4k_B = math.sqrt((x_current - (floor_x + 1)) ** 2 \
155         + (y_current - (floor_y + 1)) ** 2)
156         W1_B = 1 - d1k_B
157         W2_B = 1 - d2k_B
158         W3_B = 1 - d3k_B
159         W4_B = 1 - d4k_B
160         M1_B = crmapB[floor_x, floor_y]
161         M2_B = crmapB[floor_x + 1, floor_y]
162         M3_B = crmapB[floor_x, floor_y + 1]
163         M4_B = crmapB[floor_x + 1, floor_y + 1]
164         Mk_B[idx] = (M1_B * W1_B + M2_B * W2_B + M3_B * W3_B + M4_B * W4_B) \
165         / (W1_B + W2_B + W3_B + W4_B)
166
167         if not np.any(Mk == 0) and not np.any(Mk_B == 0):
168             break
169
170     # Check values before calculating SDLCSdata
171     if np.any(Mk <= 0) or np.any(Mk_B <= 0):
172         print(f"Simulation {sim}: Invalid values found in Mk or Mk_B.")
173         continue
174
175     Nsimv += 1 # Increment the count of valid simulations
176
177     valid_results.append(Mk)
178     for idx in range(len(Mk)):
179         Mk_components_A[idx].append(Mk[idx])
180     valid_results_B.append(Mk_B)
181     for idx in range(len(Mk_B)):
182         Mk_components_B[idx].append(Mk_B[idx])
183
184     #We create the SDLCS
185     SDLCSdata = -2.5 * (np.log(Mk_B / Mk) - np.mean(np.log(Mk_B / Mk)))
186
187     # Calculate RMS_RR for each SDLCS
188     RMS_RR = np.sqrt(np.mean(((0j - SDLCSdata) / Ej) ** 2))
189     RMS_RR_values.append(RMS_RR)
190
191     # Save SDLCS information if RMS_RR < 1.7
192     if RMS_RR < threshold:
193         valid_SDLCSdata_SDLCS.append(SDLCSdata)
194         print(f"The RMS is: {RMS_RR}")

```

```

195     print(f"The recalculated threshold is: {threshold}")
196 if RMS_RR < 2:
197     valid_SDLCdata_SDLCs_strict.append(SDLCdata)
198 if RMS_RR < min_RMS_RR:
199     min_RMS_RR = RMS_RR
200     best_SDLC = SDLCdata
201
202 #Show the results and figures for the 100000 SDLCs
203
204 print(f'Number of valid simulations: {Nsimv}')
205 print(f'The minimum RMS value is: {min_RMS_RR}')
206 # Create a histogram of RMS_RR values with a bin width of 0.5
207 bin_width = 0.5
208 bins = np.arange(0, max(RMS_RR_values) + 1, bin_width)
209 hist, edges = np.histogram(RMS_RR_values, bins=bins)
210 bin_centers = 0.5 * (edges[:-1] + edges[1:])
211
212 # Normalize the histogram
213 hist_normalized = hist / Nsimv
214
215 plt.figure(figsize=(10, 6))
216 plt.bar(bin_centers, hist_normalized, width=bin_width, align='center'\
217 , alpha=0.7, color='b')
218 plt.xlabel('RMS_RR')
219 plt.ylabel('P(RMS_RR)')
220 plt.title('Histogram of RMS_RR')
221 plt.axvline(x=1, color='r', linestyle='dashed', linewidth=2)
222 plt.axvline(x=threshold, color='r', linestyle='dashed', linewidth=2)
223
224 # Create a custom tick vector [0, 2, 5, 10, 15, 20, 30, 40, ...]
225 xticks_custom = [0, 2, 5] + list(range(10, int(max(bin_centers)) + 10, 10))
226
227 # Set the x-axis ticks using the custom vector
228 plt.xticks(xticks_custom)
229 plt.show()
230 plt.close()
231
232 # Histogram with zoom in the range [0.5, 2]
233 bin_width = 0.2
234 zoom_bins = np.arange(0.5, threshold + 1 + bin_width, bin_width)
235 zoom_hist, zoom_edges = np.histogram(RMS_RR_values, bins=zoom_bins)
236 zoom_bin_centers = 0.5 * (zoom_edges[:-1] + zoom_edges[1:])
237
238 # Normalize the zoomed histogram
239 zoom_hist_normalized = zoom_hist / Nsimv
240
241 plt.bar(zoom_bin_centers, zoom_hist_normalized, width=bin_width,\
242 align='center', alpha=0.7, color='g')
243 plt.xlabel('RMS_RR')

```

```

244 plt.ylabel('P(RMS_RR)')
245 plt.title('Histogram of RMS_RR (Zoom in [0.5, 2])')
246 plt.axvline(x=1, color='r', linestyle='dashed', linewidth=2)
247 plt.axvline(x=threshold, color='r', linestyle='dashed', linewidth=2)
248
249 # Set x-axis ticks to correspond to the range [0.5, 2]
250 plt.xticks(np.arange(1, 2.5, 0.2))
251
252 plt.savefig(zoom_histogram_path)
253 plt.show()
254 plt.close()
255
256 # Calculate the mean and standard deviation of RMS_RR
257 mean_RMS_RR = np.mean(RMS_RR_values)
258 std_RMS_RR = np.std(RMS_RR_values)
259
260 print(f'Mean RMS_RR: {mean_RMS_RR}')
261 print(f'Standard deviation of RMS_RR: {std_RMS_RR}')
262 print(f'Number of valid simulations: {Nsimv}')
263 print(f'Number of SDLCs with RMS_RR < {threshold}: {len(valid_SDLCdata_SDLCs)}')
264 print(f'Number of SDLCs with RMS_RR < 2: {len(valid_SDLCdata_SDLCs_strict)}')
265
266 # Plot and save the complete graph
267 plt.figure(figsize=(10, 6))
268 plt.errorbar(tk, Oj, yerr=Ej, fmt='o', label='ODLC Data')
269 plt.plot(tk, Oj_fit, label='ODLC Linear Fit', color='red')
270 if best_SDLC is not None:
271     plt.plot(tk, best_SDLC, label='Best SDLC', color='green')
272 plt.xlabel('tk')
273 plt.ylabel('Values')
274 plt.legend()
275 plt.title('ODLC, ODLC Linear Fit and Best SDLC')
276 plt.gca().invert_yaxis() # Invert Y-axis
277 sdlc_path = os.path.join(output_dir, 'CompleteGraph.png')
278 plt.savefig(sdlc_path)
279 plt.show()
280 plt.close()
281
282 # Plot and save the SDLC with the lowest RMS_RR along with the ODLC data
283 plt.figure(figsize=(10, 6))
284 plt.errorbar(tk, Oj, yerr=Ej, fmt='o', label='ODLC Data')
285 if best_SDLC is not None:
286     plt.plot(tk, best_SDLC, label='Best SDLC', color='green')
287 plt.xlabel('tk')
288 plt.ylabel('Values')
289 plt.legend()
290 plt.title('ODLC and Best SDLC')
291 plt.gca().invert_yaxis() # Invert Y-axis
292 sdlc_path = os.path.join(output_dir, 'GraphWithODLC.png')

```

```
293 plt.savefig(sdlc_path)
294 plt.show()
295 plt.close()
296
297 # Record the end time
298 end_time = time.time()
299
300 # Calculate the elapsed time
301 elapsed_time = end_time - start_time
302
303 # Display the elapsed time
304 print(f"Elapsed time: {elapsed_time} seconds")
```